

# Data-based theoretical identification of subcellular calcium compartments and estimation of calcium dynamics in cardiac myocytes

Leonid Livshitz<sup>1</sup>, Karoly Acsai<sup>2,3</sup>, Gudrun Antoons<sup>2,4</sup>, Karin Sipido<sup>2</sup> and Yoram Rudy<sup>1</sup>

<sup>1</sup>Cardiac Bioelectricity and Arrhythmia Centre, Washington University in St Louis, St Louis, MO, USA

<sup>2</sup>Laboratory of Experimental Cardiology, University of Leuven, Leuven, Belgium

<sup>3</sup>Division of Cardiovascular Pharmacology, Hungarian Academy of Sciences, Szeged, Hungary

<sup>4</sup>Department of Cardiology, Medical University of Graz, Graz, Austria

## Key points

- $\text{Ca}^{2+}$  release from intracellular stores affects the cardiac action potential via currents through L-type  $\text{Ca}^{2+}$  channels ( $I_{\text{Ca}}$ ) and the sodium/calcium exchanger ( $I_{\text{NCX}}$ ).
- Dynamic interactions between released calcium,  $I_{\text{Ca}}$  and  $I_{\text{NCX}}$  occur in a restricted subcellular compartment, close to  $\text{Ca}^{2+}$  released sites, where calcium concentration ( $\text{Ca}_t$ ) cannot be measured.
- We used a computational model and experimental data to define this compartment and to provide a theoretical basis for estimating  $\text{Ca}_t$ .
- We estimated  $\text{Ca}_t$  from recordings of  $I_{\text{Ca}}$  and  $I_{\text{NCX}}$  and optical recordings of whole-cell calcium concentration ( $\text{Ca}_m$ ).
- Estimated peak  $\text{Ca}_t$  ranged from  $6\ \mu\text{M}$  to  $25\ \mu\text{M}$ , depending on calcium load. Time to equilibrium between  $\text{Ca}_t$  and  $\text{Ca}_m$  was  $\sim 350$  ms. The  $\text{Ca}_t$  values are in the range of  $I_{\text{Ca}}$  and  $I_{\text{NCX}}$  sensitivity to calcium, implying that there is significant effect of  $\text{Ca}^{2+}$  in this restricted domain on their kinetics and on the action potential during cell excitation.

**Abstract** In cardiac cells,  $\text{Ca}^{2+}$  release flux ( $J_{\text{rel}}$ ) via ryanodine receptors (RyRs) from the sarcoplasmic reticulum (SR) has a complex effect on the action potential (AP). Coupling between  $J_{\text{rel}}$  and the AP occurs via L-type  $\text{Ca}^{2+}$  channels ( $I_{\text{Ca}}$ ) and the  $\text{Na}^+/\text{Ca}^{2+}$  exchanger ( $I_{\text{NCX}}$ ). We used a combined experimental and modelling approach to study interactions between  $J_{\text{rel}}$ ,  $I_{\text{Ca}}$  and  $I_{\text{NCX}}$  in porcine ventricular myocytes. We tested the hypothesis that during normal uniform  $J_{\text{rel}}$ , the interaction between these fluxes can be represented as occurring in two myoplasmic subcompartments for  $\text{Ca}^{2+}$  distribution, one (T-space) associated with RyR and enclosed by the junctional portion of the SR membrane and corresponding T-tubular portion of the sarcolemma, the other (M-space) encompassing the rest of the myoplasm.  $I_{\text{Ca}}$  and  $I_{\text{NCX}}$  were partitioned into subpopulations in the T-space and M-space sarcolemma. We denoted free  $\text{Ca}^{2+}$  concentrations in T-space and M-space  $\text{Ca}_t$  and  $\text{Ca}_m$ , respectively. Experiments were designed to allow separate measurements of  $I_{\text{Ca}}$  and  $I_{\text{NCX}}$  as a function of  $J_{\text{rel}}$ . Inclusion of T-space in the model allowed us to reproduce *in silico* the following important experimental results: (1) hysteresis of  $I_{\text{NCX}}$  dependence on  $\text{Ca}_m$ ; (2) delay between peak  $I_{\text{NCX}}$  and peak  $\text{Ca}_m$  during caffeine application protocol; (3) delay between  $I_{\text{NCX}}$  and  $\text{Ca}_m$  during  $\text{Ca}^{2+}$ -induced- $\text{Ca}^{2+}$ -release; (4) rapid  $I_{\text{Ca}}$  inactivation (within 2 ms) due to  $J_{\text{rel}}$ , with magnitude graded as a function of the SR  $\text{Ca}^{2+}$  content; (5) time delay between  $I_{\text{Ca}}$  inactivation due to  $J_{\text{rel}}$  and  $\text{Ca}_m$ . Partition of 25% NCX in T-space and 75% in M-space provided the best fit to the experimental data. Measured  $\text{Ca}_m$  and  $I_{\text{Ca}}$  or  $I_{\text{NCX}}$  were used

as input to the model for estimating  $\text{Ca}_t$ . The actual model-computed  $\text{Ca}_t$ , obtained by simulating specific experimental protocols, was used as a gold standard for comparison. The model predicted peak  $\text{Ca}_t$  in the range of 6–25  $\mu\text{M}$ , with time to equilibrium of  $\text{Ca}_t$  with  $\text{Ca}_m$  of  $\sim 350$  ms. These  $\text{Ca}_t$  values are in the range of LCC and RyR sensitivity to  $\text{Ca}^{2+}$ . An increase of the SR  $\text{Ca}^{2+}$  load increased the time to equilibrium. The  $I_{\text{Ca}}$ -based estimation method was most accurate during the ascending phase of  $\text{Ca}_t$ . The  $I_{\text{NCX}}$ -based method provided a good estimate for the descending phase of  $\text{Ca}_t$ . Thus, application of both methods in combination provides the best estimate of the entire  $\text{Ca}_t$  time course.

(Received 30 January 2012; accepted after revision 23 April 2012; first published online 30 April 2012)

**Corresponding author** Y. Rudy: Cardiac Bioelectricity and Arrhythmia Centre, Washington University in St Louis, One Brookings Drive, St Louis 63130-4899, MO, USA. Email: rudy@wustl.edu

**Abbreviations** AP, action potential; CDI,  $\text{Ca}^{2+}$ -dependent inactivation; DAD, delayed afterdepolarization; EAD, early afterdepolarization; LCC, L-type  $\text{Ca}^{2+}$  channel; NCX,  $3\text{Na}^+/\text{Ca}^{2+}$  exchanger; PMCA, plasmalemmal  $\text{Ca}^{2+}$ -ATPase pump; RDI,  $J_{\text{rel}}$ -dependent inactivation of  $I_{\text{Ca}}$ ; RyR, ryanodine receptor; SERCA, SR  $\text{Ca}^{2+}$ -ATPase pump; SR, sarcoplasmic reticulum; VDI, voltage-dependent inactivation of  $I_{\text{Ca}}$ .

## Introduction

$\text{Ca}^{2+}$  release flux ( $J_{\text{rel}}$ ) from the sarcoplasmic reticulum (SR) via ryanodine receptors (RyRs) exerts a complex effect on the cardiac action potential (AP) via  $\text{Ca}^{2+}$ -dependent inactivation of L-type  $\text{Ca}^{2+}$  channels (LCCs) (repolarizing effect) and activation of  $3\text{Na}^+/\text{Ca}^{2+}$  exchangers (NCXs) (depolarizing effect). It has been shown that abnormality of  $J_{\text{rel}}$  due to genetic defects in RyR, heart failure, or excessive phosphorylation during exercise and stress could cause abnormal cellular electrical activity and arrhythmic behaviour. For example (1) beat-to-beat alternans in  $J_{\text{rel}}$  is associated with arrhythmogenic AP alternans, with amplitude that depends on the balance between  $\text{Ca}^{2+}$  flux via LCCs ( $I_{\text{Ca}}$ ) and NCX ( $I_{\text{NCX}}$ ); this process is modulated by the  $\text{Ca}^{2+}$ /calmodulin-dependent protein kinase II (CAMKII) (Sato *et al.* 2006, Livshitz & Rudy, 2007); (2)  $I_{\text{Ca}}$  recovery from  $\text{Ca}^{2+}$ -dependent inactivation following  $J_{\text{rel}}$  is implicated in the development of early afterdepolarizations (EADs) (Antoons *et al.* 2007); and (3) diastolic  $J_{\text{rel}}$  underlies the formation of delayed afterdepolarizations (DADs) and triggered activity at high levels of  $\beta$ -adrenergic tone (e.g. Belevych *et al.* 2011; Priori & Chen, 2011).

The mechanism of coupling between  $J_{\text{rel}}$ ,  $I_{\text{NCX}}$ ,  $I_{\text{Ca}}$  and the AP is not completely understood, even under normal physiological conditions. Consensus exists that the interactions are mediated by the free  $\text{Ca}^{2+}$  sensed by these channels, and are modulated by the CAMKII signalling pathway. However, optical recordings of the whole-cell (global)  $\text{Ca}^{2+}$  transient ( $\text{Ca}_m$ ) show dynamics which correlate poorly with the much faster kinetics of the ionic currents ( $I_{\text{Ca}}$  and  $I_{\text{NCX}}$ ). This implies that these channels are experiencing different local  $\text{Ca}^{2+}$  transients ( $\text{Ca}_t$ ) that cannot be measured with current experimental techniques with sufficient

temporal and spatial resolution. Consequently, combined experimental/computational methods were developed for estimating local  $\text{Ca}^{2+}$  from measurements of whole-cell  $\text{Ca}^{2+}$  using fluorescence imaging, together with recorded  $I_{\text{NCX}}$  (Egan *et al.* 1989; Trafford *et al.* 1995; Weber *et al.* 2001) or  $I_{\text{Ca}}$  (Sipido *et al.* 1995; Sham, 1997; Zahradnikova *et al.* 2004; Antoons *et al.* 2007) as local  $\text{Ca}^{2+}$  sensors (reporters). Early work used  $\text{Ca}_m$  and mathematical modelling to calculate  $J_{\text{rel}}$  in skeletal (Melzer *et al.* 1987) and cardiac (Sipido & Wier, 1991) fibres. These indirect (inverse) methods for estimating local  $\text{Ca}^{2+}$  from  $I_{\text{NCX}}$  and  $I_{\text{Ca}}$  recordings rely heavily on the mathematical models employed and the quality of recorded  $I_{\text{NCX}}$  and  $I_{\text{Ca}}$  data.

Due to tight coupling between  $\text{Ca}^{2+}$  cycling and membrane voltage ( $V$ ) in cardiac myocytes, it is difficult to control  $I_{\text{NCX}}$  and  $I_{\text{Ca}}$  independently and separate  $\text{Ca}^{2+}$ -dependent from  $V$ -dependent processes in experiments. For example, it is extremely challenging to separate effects of  $\text{Ca}^{2+}$ -dependent (CDI) and voltage-dependent (VDI) inactivation of  $I_{\text{Ca}}$ , or effects of  $\text{Ca}^{2+}$ -dependent and voltage-dependent modulation of  $I_{\text{NCX}}$ . In addition, modulation of  $I_{\text{Ca}}$  by  $\text{Ca}^{2+}$  is due to both CDI and changes in the driving force. Moreover, there is strong interaction (mediated by  $\text{Ca}^{2+}$  changes) between  $I_{\text{Ca}}$  and  $I_{\text{NCX}}$  during an AP and therefore caution should be taken in extrapolating estimates of local  $\text{Ca}^{2+}$  from each individual current to the physiological environment of the myocyte during excitation.  $\text{Ca}^{2+}$  fluxes have been measured under experimental conditions (voltage clamp, dialysed whole cell, cocktails of blockers, non-physiological ion concentrations, artificial ion buffers, non-physiological levels of protein phosphorylation, etc.) which differ from those in intact functioning cardiac cells. Additional complexity arises from the fact that different cardiac cells (e.g. ventricular, atrial, purkinje) exhibit distinct structural organization, which is also age and species

dependent (Bootman *et al.* 2006; Soeller *et al.* 2007, 2009; Li & Rudy, 2011).

In ventricular myocytes, RyRs, NCXs and LCCs are distributed non-uniformly (Fig. 1A) in the SR membrane (RyRs) and sarcolemma (NCXs and LCCs) (Pasek *et al.* 2008; Jayasinghe *et al.* 2009; Smyrniatsa *et al.* 2010). Not all LCCs and only a fraction of NCXs sense the same  $\text{Ca}^{2+}$  as RyRs (Adachi-Akahane *et al.* 1996), underscoring the importance of considering subcellular compartments for  $\text{Ca}^{2+}$  dynamics in mathematical models of the cell. Experimental data and model simulations suggest that  $\text{Ca}^{2+}$  flux per unit time through LCCs and RyRs is several orders of magnitude greater than the diffusion flux towards the core of the cell, resulting in local subcellular  $\text{Ca}^{2+}$  gradients (Allbritton *et al.* 1992). In addition, local  $\text{Ca}^{2+}$  buffers contribute to a relatively slow (tens of milliseconds) dissipation of these  $\text{Ca}^{2+}$  gradients (Naraghi & Neher, 1997; Higgins *et al.* 2007).

Unfortunately, using numerical models of the reaction-diffusion system in the realistic, detailed geometry of the cell requires precise knowledge of the intracellular structure and of  $\text{Ca}^{2+}$  diffusion properties in this structure. It involves many parameters that cannot be constrained precisely and is computationally very demanding (e.g. Chen-Izu *et al.* 2006; Soeller *et al.* 2009).

The representation of spatial organization in a compartmental model is a simplification that makes computation possible (Atkins, 1969). It has been used extensively in modelling calcium cycling in cardiac myocytes (Standen & Stanfield, 1982; Adler *et al.* 1985; Luo & Rudy, 1994). Here, we use this approach to better define functional cellular compartments for  $\text{Ca}^{2+}$  interactions and to provide a theoretical basis for estimation of dynamic  $\text{Ca}^{2+}$  concentrations in these compartments. We hypothesize that under normal physiological conditions (i.e. uniform whole cell  $J_{\text{rel}}$ ), the interaction between  $J_{\text{rel}}$ ,  $I_{\text{Ca}}$  and  $I_{\text{NCX}}$  can be formulated, to a very good approximation, as occurring in four functional compartments of  $\text{Ca}^{2+}$  distribution, two in the myoplasm and two in the SR. One myoplasmic compartment (denoted T-space) is associated structurally with the RyRs and enclosed by the tubular portion of the sarcolemma and the junctional portion of the SR membrane (enclosed by the dashed curve in Fig. 1A). The other myoplasmic compartment (M-space) encompasses the rest of the myoplasm, enclosed by the non-tubular sarcolemma and non-junctional SR membrane. LCCs and NCXs are present in the sarcolemma of both T-space and M-space, but with different density in each compartment. We denote free  $\text{Ca}^{2+}$  concentrations in T and M spaces  $\text{Ca}_t$  and  $\text{Ca}_m$ , respectively. Similarly, the SR is also divided into two compartments of  $\text{Ca}^{2+}$  distribution. One compartment (denoted J-space) is associated structurally with the RyRs and the junctional portion of the SR membrane. The other compartment (N-space) encompasses the rest of SR

(network SR) as we have done previously (Luo & Rudy, 1994). We employ mathematical modelling together with experimental measurements to explore the interactions of  $J_{\text{rel}}$ ,  $I_{\text{Ca}}$  and  $I_{\text{NCX}}$  in the T-space and to provide a theoretical basis for estimating the  $\text{Ca}_t$  dynamic properties in this functional space, where  $J_{\text{rel}}$ ,  $I_{\text{Ca}}$  and  $I_{\text{NCX}}$  interact.

The choice of compartments was dictated by the assumptions of a uniform  $\text{Ca}^{2+}$  distribution in each compartment and a spatially uniform  $\text{Ca}^{2+}$  flux between communicating compartments. It was guided by structural and functional considerations and differs from 'subspace' and 'bulk myoplasm' used in many previous compartmental models. In these models, 'subspace' has been used to define a continuous subsarcolemmal space in the entire cell. In certain models, it was subdivided to contain a 'dyadic' space (Shannon *et al.* 2004; Higgins *et al.* 2007; Mahajan *et al.* 2008); the dyadic space communicated with the subsarcolemmal subspace, which in turn communicated with the bulk myoplasm. This implies that dyads are distributed uniformly beneath the sarcolemma, and all NCXs are affected identically by  $J_{\text{rel}}$  via a  $\text{Ca}^{2+}$  diffusion flux from the dyadic space. Based on structural and functional properties, including the non-uniform distribution and partition of LCCs and NCXs between T-tubular and non-T-tubular portions of the sarcolemma, and of RyRs in the SR membrane,  $\text{Ca}^{2+}$  distribution cannot be assumed uniform in a subsarcolemmal 'subspace' compartment. Rather, RyRs interact with LCCs and NCXs in a functional compartment near the RyR, which we label T-space. Figure 1 depicts two populations of LCCs and NCXs, one interacting with RyRs in the T-space (via a common pool of  $\text{Ca}^{2+}$ ,  $\text{Ca}_t$ ), and the other communicating directly with the M-space. Based on experimental data, we estimate the fraction of NCXs that are coupled functionally to RyRs via  $\text{Ca}_t$ .

## Methods

Symbols and definitions are given in Table 1.

## Ethical approval

All experiments were conducted at the University of Leuven, Belgium, according to the *Guide for the Care and Use of Laboratory Animals* of the National Institutes of Health (USA). Experimental protocols were approved by the ethical committee of the University of Leuven. The current study conforms to the ethical standards set by *The Journal of Physiology* (Drummond, 2009). Killing of the pigs was done under full anaesthesia (premedication with tiletamine and zolazepam, 4 mg kg<sup>-1</sup> i.m. and xylazine 0.25 mg kg<sup>-1</sup> i.m., maintenance anaesthesia with propofol i.v., 7 mg kg<sup>-1</sup> h<sup>-1</sup>); pigs were intubated and ventilated with a 1:1 oxygen–air mixture. After an additional bolus

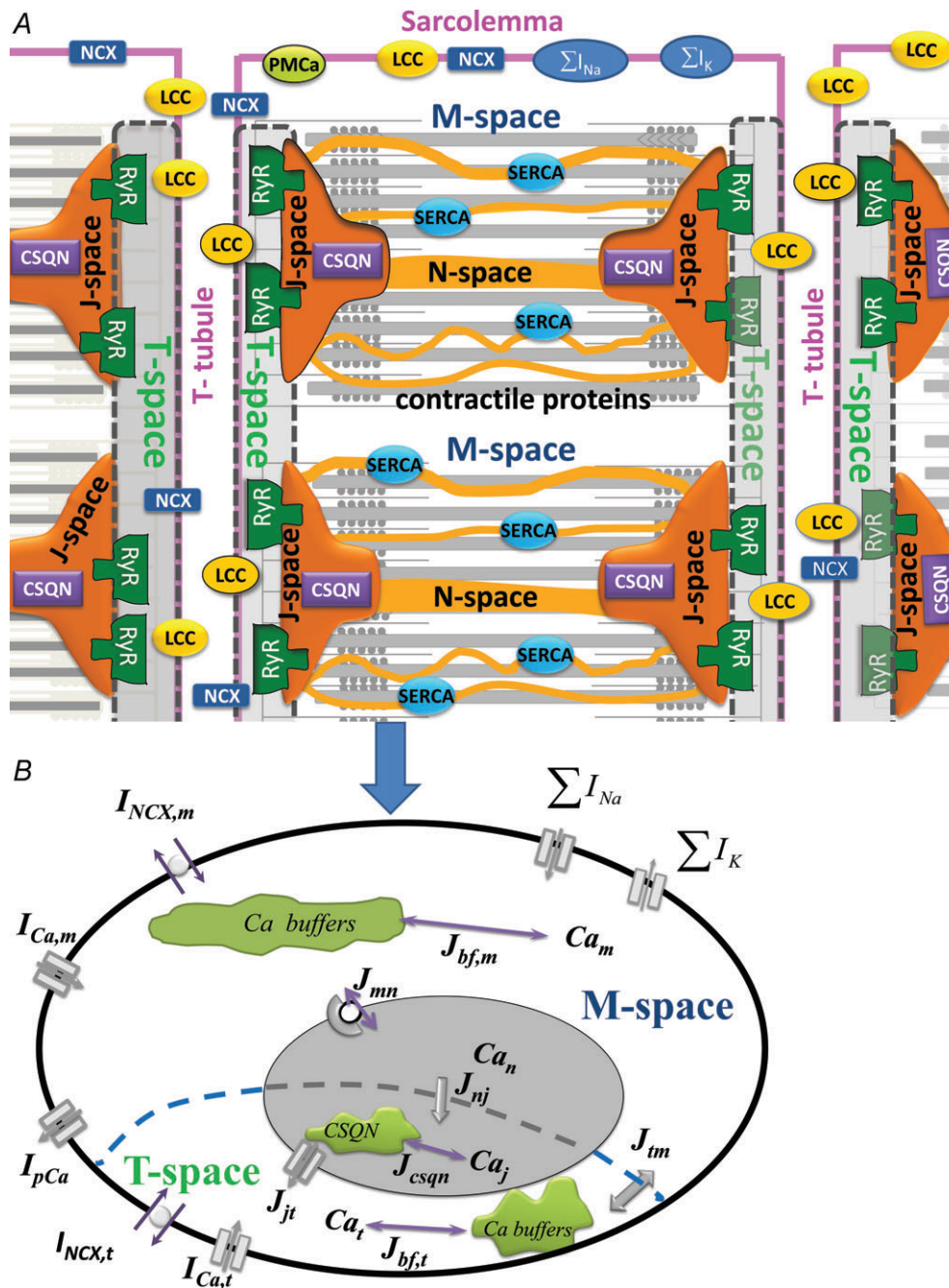


**Figure 1. Compartmental model of  $Ca^{2+}$  cycling, based on structural organization of a ventricular myocyte**

A, schematic diagram of the structural organization of a ventricular myocyte. Sarcolemmal  $Ca^{2+}$ -ATPase (PMCa), L-type  $Ca^{2+}$  channels (LCC),  $3Na^{+}/Ca^{2+}$  exchanger (NCX) and  $Ca^{2+}$  binding proteins (buffers) are expressed throughout the sarcolemma. T-Tubules run radially and flank each sarcomere.  $Ca^{2+}$  release channels (RyRs) are expressed in the junctional portion of the SR membrane which faces the T-tubular portion of the sarcolemma and bounds the calsequestrin (CSQN) containing J-spaces. The junctional portion of the SR membrane and corresponding T-tubular portion of the sarcolemma form the T-spaces (grey spaces enclosed by dashed boundaries). During uniform activation of all RyR, identical  $Ca^{2+}$  distribution can be assumed in all J-spaces and in all T-spaces. Given the structural periodicity of the myocyte, a cell average  $Ca^{2+}$  concentration in J-space ( $Ca_j$ ) and T-space ( $Ca_t$ ) can be defined. SR  $Ca^{2+}$ -ATPase (SERCA) is expressed in the network portion of the SR membrane which encloses the N-space. M-space is separated by the network portion of the SR membrane from the N-space and contains  $Ca^{2+}$  sensitive contractile (troponin) and regulatory (calmodulin) proteins.  $\Sigma I_K$  and  $\Sigma I_{Na}$  are sum of trans-sarcolemmal  $K^{+}$  and  $Na^{+}$  fluxes, respectively. B, compartmental model of  $Ca^{2+}$  cycling



Table 1. Symbols and definitions

$V$	Transmembrane potential	mV
$Ca_t$	Free $Ca^{2+}$ concentration in T-space	mm
$\overline{Ca}_t$	Inverse estimated $Ca_t$	
$Ca_m$	Free $Ca^{2+}$ concentration in M-space	
$Ca_j$	Free $Ca^{2+}$ concentration in junctional SR (J-space)	mm
$Ca_n$	Free $Ca^{2+}$ concentration in network SR (N-space)	mm
$Ca_{cmdn}$	$Ca^{2+}$ bound to calmodulin in M-space	mm
$Ca_{csqn}$	$Ca^{2+}$ bound to calsequestrine in J-space	mm
$Ca_{trpn}$	$Ca^{2+}$ bound to troponin in M-space	mm
$Ca_{b,f}$	$Ca^{2+}$ bound to fast buffer in T-space	mm
$Ca_{b,s}$	$Ca^{2+}$ bound to slow buffer in T-space	mm
$J_{Ca,m}$	Trans-sarcolemmal $Ca^{2+}$ flux in M-space	mm ms <sup>-1</sup>
$J_{Ca,t}$	Trans-sarcolemmal $Ca^{2+}$ flux in T-space	mm ms <sup>-1</sup>
$J_{nj}$	$Ca^{2+}$ between N-space to J-space	mm ms <sup>-1</sup> s
$\tau_{tr}$	Time constant of $J_{nj}$	ms
$J_{tm}$	$Ca^{2+}$ flux between T-space and M-space	mm ms <sup>-1</sup> s
$\tau_{diff}$	Time constant of $J_{tm}$	ms
$J_{mn}$	$Ca^{2+}$ flux between M-space and N-space	mm ms <sup>-1</sup>
AP	Action potential	
$I_{Ca}$	L-type $Ca^{2+}$ current	$\mu A \mu F^{-1}$
$f_{Ca}$	$Ca^{2+}$ -dependent inactivation gate of $I_{Ca}$	
$\overline{f}_{Ca}$	Inverse estimated $f_{Ca}$	
$\beta$	Fraction of NCX in T-space	
$I_{NCX}$	$Na^+$ - $Ca^{2+}$ exchanger current	$\mu A \mu F^{-1}$
$NCX_{max}$	Maximal turnover rate of $I_{NCX}$	$\mu A \mu F^{-1}$
$K_{NCX}$	$I_{NCX}$ affinity to $Ca^{2+}$	mm
$I_{Ca}^0$	$I_{Ca}$ in the absence of $J_{rel}$	$\mu A \mu F^{-1}$
$\Delta I_{Ca} = I_{Ca} - I_{Ca}^0$	Difference current (presence-absence of $J_{rel}$ )	
$t_{max}$	Time of maximal $\Delta I_{Ca}$	ms
$I_{pCa}$	$Ca^{2+}$ current via PMCA	$\mu A \mu F^{-1}$
$I_{Cab}$	Background $Ca^{2+}$ current	$\mu A \mu F^{-1}$
$J_{rel}$	$Ca^{2+}$ flux via RyRs	mm ms <sup>-1</sup>
$\sum I_{Na}$	Sum of transsarcolemmal $Na^+$ fluxes	mm ms <sup>-1</sup>
$\sum I_K$	Sum of transsarcolemmal $K^+$ fluxes	mm ms <sup>-1</sup>
$J_{SERCA}$	$Ca^{2+}$ flux via SERCA	mm ms <sup>-1</sup>
$J_{leak}$	$Ca^{2+}$ leak flux from J-space	mm ms <sup>-1</sup>
$J_{b,x}$	$Ca^{2+}$ flux from and to $Ca^{2+}$ buffers 'x'	mm ms <sup>-1</sup>
$V_x$	Volume of compartment 'x'	$\mu l$
$C_m, C_t$	M-space and T-space capacitances of sarcolemma, $\mu F$	
$F$	Faraday constant, 96,487 C mol <sup>-1</sup>	
$R$	Gas constant, 8314 J mmol <sup>-1</sup> K <sup>-1</sup>	
$T$	Temperature, 310 K	
$Na_o$	External $Na^+$ concentration	
$Ca_o$	External $Ca^{2+}$ concentration	

based on the structural organization in panel A, when synchronized activation of RyR generates a uniform  $Ca^{2+}$  flux ( $J_{jt}$ ) from J-space to T-space. The transsarcolemmal  $Ca^{2+}$  fluxes, which include currents via LCC ( $I_{Ca}$ ) and NCX ( $I_{NCX}$ ), are partitioned between T-space and M-space. The effects of the contractile and regulatory proteins on  $Ca^{2+}$  dynamics is accounted for by buffering fluxes in the M-space ( $J_{bf,m}$ ), T-space ( $J_{bf,t}$ ), and J-space ( $J_{csqn}$ ).  $Ca^{2+}$  flux between M-space and N-space ( $J_{mn}$ ) is carried by SERCA. Transfer of  $Ca^{2+}$  between T-space and M-space ( $J_{tm}$ ) is proportional to the difference between  $Ca_t$  and  $Ca_m$ . Similarly,  $J_{nj}$  is proportional to the difference between  $Ca_n$  and  $Ca_j$ . Additional symbols are defined in the text. Computer code is available on the website <http://rudylab.wustl.edu/research/cell/lrd2.htm>.

of pentobarbital ( $100 \text{ mg kg}^{-1}$  i.m.), hearts were excised quickly and placed in oxygenated Tyrode solution.

### Experimental considerations

The experiments were conducted in porcine ventricular myocytes and described in detail in Acsai *et al.* (2011). Briefly, experiments were designed to allow separate measurements of  $I_{\text{Ca}}$  and  $I_{\text{NCX}}$  as a function of  $J_{\text{rel}}$ , which was controlled by regulation of SR  $\text{Ca}^{2+}$  load using caffeine and voltage-clamp protocols. Whole-cell  $\text{Ca}^{2+}$  was measured optically. The size of the T-space compartment is orders of magnitude smaller than that of the M-space. Therefore, contribution from  $\text{Ca}_t$  to the optically measured  $\text{Ca}^{2+}$  signal can be regarded as negligible and the cell-average  $\text{Ca}^{2+}$  signal reflects  $\text{Ca}_m$ . The experimental protocols were conducted under voltage clamp conditions, with all ion concentrations, except  $\text{Ca}^{2+}$ , maintained constant. In addition, we utilized a depolarizing step to  $+10 \text{ mV}$  which ensures maximal spatially uniform activation of  $J_{\text{rel}}$  to reflect normal conditions in non-failing myocytes (see Fig. 2A in Acsai *et al.* 2011). In addition, large concentrations of caffeine were used ( $10 \text{ mM}$ ) to ensure spatial uniformity of caffeine-evoked  $J_{\text{rel}}$ . Also, the state of the cell (SR  $\text{Ca}^{2+}$  load, depolarizing  $V$  pulses) in both the  $I_{\text{Ca}}$  and  $I_{\text{NCX}}$  experiments was identical to yield identical estimations of  $\text{Ca}_t$ . Experimental recordings of  $I_{\text{Ca}}$ ,  $\text{Ca}_m$  and  $I_{\text{NCX}}$  were used as an input to the model for estimating  $\text{Ca}_t$ ; the mathematical formulation and simulation procedures are described below.

**Myocyte isolation.** In the current study we used ventricular myocytes isolated from the mid-myocardial layer of the posterior wall of healthy pigs. Animals ( $n = 12$ , weight  $35\text{--}45 \text{ kg}$ ) were housed and treated according to the *Guide for the Care and Use of Laboratory Animals* (National Institutes of Health, USA) and experimental protocols were approved by the in-house ethical committee at the University of Leuven. Killing of the pigs was done under full anaesthesia, hearts were excised quickly and placed in oxygenated Tyrode solution. The circumflex coronary artery was cannulated and the myocardium was perfused with  $\text{Ca}^{2+}$ -free Tyrode solution and subsequently enzyme solution. Isolated cells were stored at room temperature and used within 12 h. The isolation procedure was as described before (Heinzel *et al.* 2002).

**Chemical solutions.** Chemicals were purchased from Sigma, fluorescent probes from Invitrogen, Belgium. Tyrode solution for cell storage contained (in mM) NaCl 130, KCl 5.4, Hepes 11.8,  $\text{MgCl}_2$  0.5,  $\text{CaCl}_2$  1.8, and glucose 10, pH 7.40 with NaOH. For recording  $I_{\text{CaL}}$  and  $I_{\text{NCX}}$ , the extracellular solution contained (in mM): NaCl

130, CsCl 10, Hepes 11.8,  $\text{MgCl}_2$  0.5,  $\text{CaCl}_2$  1.8, glucose 10, pH 7.4 adjusted with NaOH. To block the fast  $\text{Na}^+$  current,  $200 \mu\text{M}$  lidocaine was included in the external solution. In order to increase the amplitude of the  $I_{\text{CaL}}$  and facilitate study of  $\text{Ca}^{2+}$ -dependent inactivation and recovery by increasing SR  $\text{Ca}^{2+}$  content,  $5 \mu\text{M}$  forskolin was added to the external solution. The pipette solution contained (in mM): caesium aspartate 120, TEACl 10, NaCl 5, Hepes 10,  $\text{MgCl}_2$  0.5, MgATP 5, pH 7.2 adjusted with CsOH with  $50 \mu\text{M}$  K5Fluo-3 was added as a fluorescent  $\text{Ca}^{2+}$  indicator for measurement of the global cytosolic  $\text{Ca}^{2+}$  concentration. In the experiments carried out in  $\text{Na}^+$  free conditions, the external solution contained *N*-methyl-D-glucamine 120, TEACl 20, Hepes 11,  $\text{MgCl}_2$  0.5,  $\text{CaCl}_2$  1.8, glucose 10, pH 7.4 with HCl.

Cardiac myocytes were placed in a perfusion chamber on an inverted microscope (Nikon Diaphot). The set-up for epifluorescence recording, calibration of the  $\text{Ca}^{2+}$ -dependent fluorescence and measurement of membrane currents were as described previously (Acsai *et al.* 2011). Fluorescence signals were recorded from the entire cell and calibrated to  $[\text{Ca}^{2+}]$  after obtaining  $F_{\text{max}}$  at the end of the experiments. All experiments were performed at  $36^\circ\text{C}$ .

### Model geometry and calcium compartments

Typical spatial organization of a non-failing ventricular myocyte is shown in Fig. 1A. The cell membrane (sarcolemma) invaginates to form transverse tubules (T-tubule) which run predominantly radially across the muscle fibre. These tubules are situated between the sarcomeres, which consist of a regular array of  $\text{Ca}^{2+}$  binding myofilaments, forming the basic unit of the contractile machinery (Adrian, 1983; Bootman *et al.* 2006). Given the structural periodicity of the myocyte, only two sarcomeres in the radial direction (out of many) are shown. Approximately half of the sarcolemmal surface area is associated with the T-tubular system, where LCCs and NCXs are expressed at higher density.  $\text{Ca}^{2+}$ -binding calsequestrin (CSQN) and RyRs are expressed in the J-space membrane and lumen, respectively. SR  $\text{Ca}^{2+}$ -ATPase (SERCA) is expressed in the N-space membrane, in close proximity to the contractile proteins in the myoplasm.

When all RyRs are activated in synchrony to generate  $J_{\text{rel}}$  flux from J-spaces to T-spaces, uniform  $\text{Ca}^{2+}$  distributions can be assumed in these compartments and represented in the model by average  $\text{Ca}_j$  and  $\text{Ca}_t$  (Fig. 1A and B).

### Compartmental model based on structural organization of a ventricular myocyte

A schematic diagram of the model is shown in Fig. 1B. The Luo–Rudy dynamic (LRd) model (Luo & Rudy,

1994) was used as the template for modelling  $\text{Ca}^{2+}$  cycling; it was modified to fit porcine data, as experiments were conducted in porcine myocytes. The LRd model includes three intracellular  $\text{Ca}^{2+}$  compartments (myoplasm, network SR and junctional SR). Each compartment is characterized functionally by the bound and free  $\text{Ca}^{2+}$  concentrations, and  $\text{Ca}^{2+}$  fluxes in and out of the compartment (Hund & Rudy, 2004; Faber *et al.* 2007). Bound  $\text{Ca}^{2+}$  in each compartment is associated with endogenous  $\text{Ca}^{2+}$  buffers. For the purpose of this study (and to better represent the structural organization of a ventricular myocyte), the original myoplasmic  $\text{Ca}^{2+}$  compartment of the LRd model was subdivided into two compartments: T-space and M-space (Fig. 1B). Following Winka *et al.* (1999), we assumed that SR calcium is divided between two functionally discrete pools, one is available for release during normal  $I_{\text{Ca}}$ -triggered  $J_{\text{rel}}$  (J-space), while the other is releasable by caffeine application but unavailable for release during normal triggered release (N-space).

Also, note that the T-space is not separated by a membrane from the M-space (nor is J-space from N-space); rather, they are separated functionally by  $\text{Ca}^{2+}$  diffusion barriers which result in faster and larger  $\text{Ca}^{2+}$  transients in the T-space (J-space) than in the M-space (N-space).  $\text{Ca}^{2+}$  diffusion barriers between T-space and M-space and between J-space and N-space (dashed curve, Fig. 1B) are accounted for by diffusion fluxes  $J_{\text{tm}}$  and  $J_{\text{nj}}$ , respectively.

### The mathematical model

Free  $\text{Ca}^{2+}$  concentration (mM) in T-space, M-space, N-space and J-space are denoted  $\text{Ca}_t$ ,  $\text{Ca}_m$ ,  $\text{Ca}_n$  and  $\text{Ca}_j$ , respectively.  $\text{Ca}^{2+}$  efflux from compartment 'x' to compartment 'y' ( $J_{xy}$ ) has units of millimolar of x volume ( $v_x$ ) per ms. Consequently, to ensure  $\text{Ca}^{2+}$  conservation,  $\text{Ca}^{2+}$  influx into compartment y is normalized by the volume fractions  $v_{xy} = v_x/v_y$ . The balance of fluxes for each compartment in terms of free  $\text{Ca}^{2+}$  concentrations is as follows:

$$\begin{aligned}\frac{d\text{Ca}_t}{dt} &= J_{\text{Ca},t} + v_{jt} \cdot J_{jt} - J_{\text{tm}} - J_{\text{bf},t} \\ \frac{d\text{Ca}_m}{dt} &= J_{\text{Ca},m} + v_{tm} \cdot J_{\text{tm}} - J_{\text{mn}} - J_{\text{bf},m} \\ \frac{d\text{Ca}_n}{dt} &= v_{mn} \cdot J_{\text{mn}} - J_{\text{nj}} \\ \frac{d\text{Ca}_j}{dt} &= v_{nj} \cdot J_{\text{nj}} - J_{jt} - J_{\text{csqn}}\end{aligned}\quad (1)$$

where subscripts t, m, n, and j indicate the corresponding quantities for T-space, M-space, N-space and J-space, respectively. Trans-sarcolemmal  $\text{Ca}^{2+}$  fluxes into M-space and T-space are denoted

$J_{\text{Ca},m} = \psi_m(I_{\text{Ca},m} + I_{\text{Cab},m} + I_{\text{pCa},m} - 2I_{\text{NCX},m})$  and  $J_{\text{Ca},t} = \psi_t(I_{\text{Ca},t} + I_{\text{Cab},t} + I_{\text{pCa},t} - 2I_{\text{NCX},t})$ , respectively.  $\psi_m = -C_m/(2v_mF)$  and  $\psi_t = -C_t/(2v_tF)$  are  $\text{Ca}^{2+}$  current to flux conversion factors for T-space and M-space, respectively.  $F = 96,485$  is the Faraday constant. Membrane capacitance in M-space ( $C_m$ ) and T-space ( $C_t$ ) is the same.  $I_{\text{pCa}}$  is current via PMCA (plasma membrane ATPase) and  $I_{\text{Cab}}$  is background leak current (Livshitz & Rudy, 2009).

M-space and T-space, and N-space and J-space communicate via diffusion fluxes,  $J_{\text{tm}} = (\text{Ca}_t - \text{Ca}_m)/\tau_{\text{diff}}$  ( $v_{tm} = v_t/v_m \approx 0.0152$ ) and  $J_{\text{nj}} = (\text{Ca}_n - \text{Ca}_j)/\tau_{\text{tr}}$  ( $v_{nj} = v_n/v_j \approx 11.5$ ), respectively.  $\text{Ca}^{2+}$  flux between J-space and T-space ( $J_{jt}$ ) has two components,  $J_{\text{rel}}$  and  $J_{\text{leak}}$ . Formulations of these fluxes are provided in the Appendix eqn (A2).

$\text{Ca}^{2+}$  binding sites (buffers) are defined in terms of  $\text{Ca}^{2+}$  fluxes between a buffer and its corresponding compartment ( $J_{\text{bf},m}$ ,  $J_{\text{bf},t}$  and  $J_{\text{csqn}}$  in Fig. 1B). In M-space,  $J_{\text{bf},m}$  includes a fast component (calmodulin) and a slow component (troponin). Similarly,  $J_{\text{bf},m}$  in T-space has fast ( $J_{\text{b},f}$ ) and slow ( $J_{\text{b},s}$ )  $\text{Ca}^{2+}$  anionic binding sites.  $J_{\text{mn}}$  is carried by SERCA. Formulations of fluxes are provided in the Appendix eqns (A1)–(A3).

**Parametrization of the model.** Experimental data were used to fit the model parameters, including the activation and inactivation kinetics of  $I_{\text{Ca}}$ , partition of NCX between the T and M spaces, density of  $\text{Ca}^{2+}$  binding sites on the SR membrane and sarcolemma, calmodulin partition between the T and M compartments, and intra-compartmental  $\text{Ca}^{2+}$  diffusion rates. Whenever possible, we used different sets of experimental data for the forward model validation and for inverse model estimation. The parameter  $\tau_{\text{tr}}$  (200–600 ms) was set to reproduce experimentally measured  $\text{Ca}_m$  restitution (Luo & Rudy, 1994). The time constant of  $\text{Ca}^{2+}$  flux between the T-space and M-space was fitted to reproduce the experimentally observed delay between peak  $\text{Ca}_m$  and the onset of  $I_{\text{Ca}}$  inactivation due to  $J_{\text{rel}}$ . The parameter  $\tau_{\text{diff}}$  (0.1–0.2 ms) and T-space buffering parameters were set to reproduce the experimentally measured rate of rise of  $\text{Ca}_m$  (4–8 mM ms<sup>-1</sup>, as in Sipido & Wier (1991)) and its time to peak. Several model parameters, such as compartment volumes and total concentrations of  $\text{Ca}^{2+}$  buffers, were constrained by conservation of total  $\text{Ca}^{2+}$  in the cell.

The state variables of the model are membrane voltage, free ion concentrations, and ion channels gating variables. Computation of ionic currents (e.g.  $I_{\text{Ca}}$  and  $I_{\text{NCX}}$ ) from these state variables constitutes a forward problem. Estimation of  $\text{Ca}_t$  (the estimate is denoted  $\overline{\text{Ca}}_t$ ) from  $\text{Ca}_m$  together with  $I_{\text{Ca}}$  or  $I_{\text{NCX}}$  constitutes an inverse problem (Keller, 1976). Note that  $\text{Ca}_m$ ,  $I_{\text{Ca}}$  or  $I_{\text{NCX}}$  can be either measured experimentally or generated by the model in a

forward simulation. In the approach presented here, the forward-calculated  $\text{Ca}_t$  (obtained by simulating specific experimental protocols *in silico*) is used as a standard for comparison and evaluation of  $\overline{\text{Ca}_t}$ . This allows us to critically validate and evaluate different experimental methods and protocols that have been used to estimate  $\text{Ca}_t$ .

It should be noted that the sensitivity of the inverse model to variations in parameter values is much greater than that of the forward model, especially at saturating levels of  $\text{Ca}^{2+}$ .

**Current through L-type  $\text{Ca}^{2+}$  channels,  $I_{\text{Ca}}$ .** LCCs were partitioned between the T-space and M-space, with a large fraction (85–95%) in T-space; total  $I_{\text{Ca}} = I_{\text{Ca},m} + I_{\text{Ca},t}$ . We assumed that the intrinsic LCC properties are independent of their location and dropped the subscripts *m* and *t* for notational convenience. The L-type channel current is as in Luo & Rudy (1994):

$$I_{\text{Ca}} = P_{\text{Ca}} E_{\text{Ca}} d \cdot f \cdot f_{\text{Ca}} \quad (2)$$

where  $P_{\text{Ca}}$  is the maximal conductance,  $d$  is a  $V$ -dependent activation gate,  $f$  is a  $V$ - and  $\text{Ca}^{2+}$ -dependent inactivation gate, and  $f_{\text{Ca}}$  is a  $\text{Ca}^{2+}$ -dependent inactivation gate.  $E_{\text{Ca}}$  denotes the driving force for  $\text{Ca}^{2+}$  flux through the LCC as a function of trans-sarcolemmal  $\text{Ca}^{2+}$  and  $V$  gradients, given by the Goldman–Hodgkin–Katz relation (GHK) (Hille, 2001),

$$E_{\text{Ca}} = 4V\varphi F(\text{Ca}\gamma_{\text{Ca}}e^{V\varphi} - \gamma_{\text{Ca}o}\text{Ca}_o)/(e^{V\varphi} - 1) \quad (3)$$

where  $\varphi = F/RT = 0.0374 \text{ (V}^{-1}\text{)}$ ,  $R = 8314 \text{ (J mol}^{-1} \text{ K}^{-1}\text{)}$  is the universal gas constant,  $T = 310$  is the absolute temperature (K), and  $\gamma_{\text{Ca}}$  and  $\gamma_{\text{Ca}o}$  are activity coefficients for free intracellular (Ca) and extracellular ( $\text{Ca}_o$ ) concentrations, respectively. By definition  $\gamma_{\text{Ca}i} > \gamma_{\text{Ca}o}$  if  $\text{Ca} < \text{Ca}_o$ .  $\gamma_{\text{Ca}}\text{Ca}_i$  can be viewed as an effective concentration of  $\text{Ca}^{2+}$  (Hille, 2001).  $I_{\text{Ca}}$  inactivation is represented by the product of two time-dependent processes: (1) voltage-dependent inactivation modulated by free  $\text{Ca}^{2+}$  ions,  $f$ -gate, and (2) a  $\text{Ca}^{2+}$ -dependent process,  $f_{\text{Ca}}$ -gate.

**Steady-state voltage dependence of  $I_{\text{Ca}}$  activation ( $d$ -gate).** Formulation of the voltage-dependent activation  $d$ -gate was derived using peak values of  $I_{\text{Ca}}$  measured in porcine ventricular myocytes (Stengl *et al.* 2010).  $I_{\text{Ca}}$  elicited by test voltage pulses was normalized by the driving force  $E_{\text{Ca}}$  (eqn (3)) at each voltage step. A best-fit analytical expression for steady-state  $d_{\infty}$  was obtained using the Matlab (The Mathworks, Natick, MA,

USA) subroutine ‘lsqcurvefit’ and is as follows:

$$d_{\infty} = I_{\text{Ca,peak}}/E_{\text{Ca}} \\ = \frac{1}{(1 + e^{-(V-16)/13.6})(1 + e^{-(V+5.97)/5.15})} \quad (4)$$

Supplemental Fig. S1A shows simulated (continuous trace) and measured (circles)  $I$ – $V$  curves. Supplemental Fig. S1B shows model simulated  $d_{\infty}$  (eqn (4), continuous black curve).  $\text{Ca}^{2+}$  was set to  $0.1 \mu\text{M}$  in these simulations. The time constant of  $I_{\text{Ca}}$  activation,  $\tau_d$ , is fast and was set to its average value of 1 ms (Luo & Rudy, 1994).

**Steady-state dependence of  $f$ -gate on  $V$  and  $\text{Ca}^{2+}$ .** Following Morad & Soldatov (2005) we assumed that  $I_{\text{Ca}}$  inactivation is  $V$ -dependent and is not complete in the absence of  $\text{Ca}^{2+}$

$$f_{\infty} = (1 - a_v)f_{V\infty} - a_v f_{V\text{Ca}\infty} \\ = \frac{(1 - a_v)}{1 + e^{(V+32)/8}} + a_v - \frac{a_v}{1 + \text{Ca}_i/K_{V\text{Ca}}} \quad (5)$$

$0 < a_v < 1$  is a factor that defines the contribution of  $\text{Ca}^{2+}$  ( $f_{V\text{Ca}\infty}$ ) and voltage ( $f_{V\infty}$ ) to steady-state  $f_{\infty}$ . Typically,  $a_v$  was set to 0.25.  $f_{V\infty}$  and  $f_{V\text{Ca}\infty}$  are saturating functions of  $V$  and  $\text{Ca}^{2+}$ , respectively.  $K_{V\text{Ca}} = 3\text{--}5 \mu\text{M}$  is a half-saturation coefficient. Supplemental Fig. S1B shows measured (circles) and simulated (grey curve)  $f_{V\infty}$  (Stengl *et al.* 2010). Note that  $a_v$  was set to 0 in this simulation.

**Time-constant of  $I_{\text{Ca}}$  inactivation ( $\tau_f$ ) with  $\text{Ca}^{2+}$ -dependent acceleration.** We assumed that  $I_{\text{Ca}}$  inactivation is  $V$  dependent and is accelerated in the presence of  $\text{Ca}^{2+}$ :

$$\tau_f = \tau_{fV} - \tau_{fV\text{Ca}} = 66 + \frac{(V - 8.73)^2}{11.72 + 0.05V} - \frac{\text{Ca}_{V\tau}}{1 + K_{V\tau\text{Ca}}/\text{Ca}_i} \quad (6)$$

$\tau_{fV\text{Ca}}$  is a  $\text{Ca}^{2+}$ -dependent acceleration factor; its maximal value equals  $\text{Ca}_{V\tau} = 55$  ms, and half-saturation constant  $K_{V\tau\text{Ca}} = 1 \mu\text{M}$ . The best fit of  $\tau_f$  ( $V$ -dependent term in eqn (6)) to experimental data is shown in Supplemental Fig. S1C. In the simulations,  $\tau_f$  values beyond experimentally recorded voltages (i.e. more than 40 mV and less than  $-10$  mV) were set to 143 ms and 95 ms, respectively.  $\text{Ca}_{V\tau}$  was set to zero in the simulation of Fig. S1C.

**$\text{Ca}^{2+}$ -dependent inactivation gate  $f_{\text{Ca}}$ .** Steady-state ( $f_{\text{Ca}\infty}$ ) and time constant ( $\tau_{f\text{Ca}}$ ) of  $\text{Ca}^{2+}$ -dependent inactivation were formulated as follows:

$$f_{\text{Ca},\infty} = \frac{1}{1 + \text{Ca}_i/K_{f\text{Ca}}}, \\ \tau_{f\text{Ca}} = \frac{0.2}{0.01 + 4\text{Ca}_i} + \frac{0.1}{4 + 0.01/\text{Ca}_i} \quad (7)$$



where  $K_{fCa} = 4 \mu\text{M}$  is the half-saturation constant. Parameters in eqns (6) and (7) were fitted to reproduce the time course of  $I_{Ca}$  with and without  $J_{rel}$ . Supplemental Fig. S1D shows a measured trace of  $I_{Ca}$  just after caffeine application (i.e. depleted SR  $\text{Ca}^{2+}$ ) (dotted grey trace) and for a  $\text{Ca}^{2+}$  loaded SR (dotted black trace). Comparison of the  $I_{Ca}$  traces shows significant acceleration of inactivation and decrease of peak  $I_{Ca}$  due to  $J_{rel}$ . In addition, a long lasting effect of  $J_{rel}$  on the  $I_{Ca}$  time course is observed even after 60 ms. These features are well replicated by the  $I_{Ca}$  model (see continuous traces in Supplemental Fig. S1D).

### $\text{Ca}_t$ estimation using $J_{rel}$ modulation of $I_{Ca}$

Estimation of free  $\text{Ca}^{2+}$  in the T-space requires formulation of its estimate,  $\overline{\text{Ca}}_t$ , as a function of  $J_{rel}$ -dependent inactivation (RDI) of  $I_{Ca}$ . Assuming that  $J_{rel}$  is the major  $\text{Ca}^{2+}$  flux that contributes to  $\text{Ca}_t$ , the kinetics of  $I_{Ca}$  inactivation in the presence of different RDI levels could be used to estimate  $\text{Ca}_t$ . We assume that RDI is a saturating function of  $\text{Ca}^{2+}$ , denoted  $\overline{f}_{Ca}$ , with a half-saturation constant  $K_{\Delta fCa}$ . With this assumption,  $\overline{\text{Ca}}_t$  is given by:

$$\overline{\text{Ca}}_t = \frac{K_{\Delta fCa}(1 - \overline{f}_{Ca})}{\overline{f}_{Ca}} \quad (8)$$

RDI is a very fast process, with a time constant less than 4 ms (Antoons *et al.* 2007); thus, an instantaneous relation between  $\text{Ca}_t$  and  $\overline{f}_{Ca}$  was assumed. Note that the estimation of  $\text{Ca}_t$  using eqn (8) does not depend on the protocol used for estimating  $\overline{f}_{Ca}$ . To estimate  $\overline{f}_{Ca}$ , we utilized the protocol of Acsai *et al.* 2011, shown in Fig. 2. Briefly, after depletion of SR  $\text{Ca}^{2+}$  with caffeine, the cell was repeatedly stimulated with a voltage pulse of duration 200 ms (i.e. typical AP duration, APD), from a holding potential  $V_h$  (−70 mV) to a depolarized potential  $V_d$  (10 mV). The magnitude and time course of the resulting  $I_{Ca}$  were influenced by VDI and CDI. However, the difference between the first  $I_{Ca}$  trace immediately after caffeine application (black trace, denoted  $I_{Ca}^0$ ) and the following traces of  $I_{Ca}$  ( $\Delta I_{Ca} = I_{Ca} - I_{Ca}^0$ ) reflects  $I_{Ca}$  inactivation due to  $J_{rel}$  only. Note that due to the long (>4 s) interpulse interval, no accumulation of diastolic  $\text{Ca}^{2+}$  was detected, i.e. the initial phases of  $\text{Ca}_m$  (<10 ms) were almost identical for all pulses. This implies that most of the  $\text{Ca}^{2+}$  that entered through LCCs during the 200 ms depolarizing voltage pulses was sequestered by the SR and did not contribute directly to  $I_{Ca}$  inactivation. The decline of  $I_{Ca}$  was therefore attributed to an augmented  $J_{rel}$  due to increased SR  $\text{Ca}^{2+}$  load with each consecutive pulse. Thus, in forward model simulations (Fig. 2, bottom panels) we generated the data using different (graded) initial values of SR  $\text{Ca}^{2+}$  content ( $\text{Ca}_j = \text{Ca}_n$ ) to modulate  $J_{rel}$  and, in turn,  $I_{Ca}$ . Note that zero SR  $\text{Ca}^{2+}$  content ( $\text{Ca}_n = \text{Ca}_j = 0$ )

corresponds to experimental conditions after caffeine application. Other  $\text{Ca}_j$  values were varied from 0.62 to 1.3 mM. As was shown previously (e.g. Shannon *et al.* 2004) and modelled in this study (eqn (A2)),  $J_{rel}$  is a steep non-linear function of the SR  $\text{Ca}^{2+}$  content. Therefore, relatively small changes in  $\text{Ca}_j$  result in large changes of  $J_{rel}$ . The time course of  $\text{Ca}^{2+}$  in the J-space and N-space is shown in Supplemental Fig. S2.

In the protocol of Fig. 2, any effect due to a small fraction of  $\text{Ca}^{2+}$  carried via LCCs in the M-space was eliminated by the  $I_{Ca}^0$  subtraction procedure. Because  $J_{rel}$  is much larger (10 times; see Fig. 3B) than  $J_{CaT}$ ,  $\Delta I_{Ca}$  is a good surrogate for the time-dependent  $\text{Ca}_t$  transient. To convert  $\Delta I_{Ca}$  into the dimensionless units of  $\overline{f}_{Ca}$ , we normalized it by the value of  $I_{Ca}^0$  when  $\Delta I_{Ca}$  was maximal:

$$\overline{f}_{Ca} = 1 - \frac{\Delta I_{Ca}}{I_{Ca}^0(t_{\Delta \max})} \quad (9)$$

where  $I_{Ca}^0(t_{\Delta \max})$  is the value of  $I_{Ca}^0$  at the time ( $t_{\Delta \max}$ ) when the effect of  $J_{rel}$  on the  $I_{Ca}$  time course is maximal. This normalization procedure eliminates a possible effect of the time onset of  $J_{rel}$  on the relative contribution of

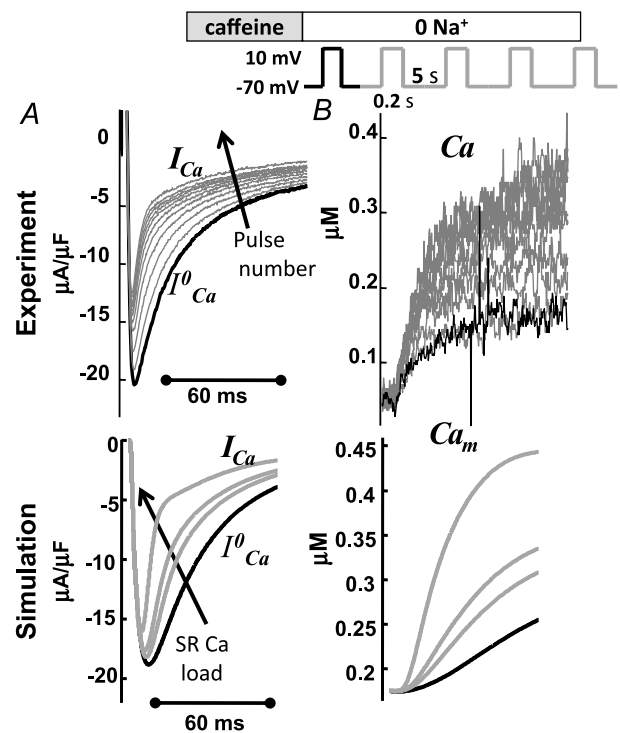


**Figure 2.  $\text{Ca}_m$  and  $I_{Ca}$  inactivation increase with increasing SR load**

A, superimposed traces of  $I_{Ca}$  evoked by depolarizing pulses to 10 mV for 200 ms (inset on top show the experimental protocol). B, corresponding traces of the global  $\text{Ca}^{2+}$  transient ( $\text{Ca}_m$ ). Experimental recordings are shown at the top, model simulations at the bottom. The first trace of  $I_{Ca}$  and of  $\text{Ca}_m$  after caffeine application (i.e. for depleted SR) is depicted in black. Arrows indicate increasing number of depolarizing pulses.

$\text{Ca}^{2+}$  and  $V$  to  $I_{\text{Ca}}$  inactivation. Previously,  $\Delta I_{\text{Ca}}$  was normalized by peak  $I_{\text{Ca}}^0$ ; we will discuss the benefits of the new normalization procedure in connection with Fig. 7. It is clear from eqn (8) that in order to accurately estimate  $\overline{\text{Ca}}_t$ ,  $K_{\text{fca}}$  must be known with sufficient accuracy. Values of  $f_{\text{Ca}}$  affinity to  $\text{Ca}^{2+}$  (which is largely dependent on calmodulin affinity to  $\text{Ca}^{2+}$ ) were reported in the range 2–10  $\mu\text{M}$  (Saucerman & Bers, 2012); we set the value of  $K_{\text{fca}} = K_{\text{fCa}} = 4 \mu\text{M}$ .

**$\text{Ca}_t$  estimation using  $I_{\text{NCX}}$  and  $\text{Ca}_m$ : forward and inverse relations between  $I_{\text{NCX}}$ ,  $\text{Ca}_m$  and  $\text{Ca}_t$ .** Experimental data suggest that  $I_{\text{NCX}}$  is a saturating function of the intracellular  $\text{Ca}^{2+}$  concentration, at given values of  $V$  and other ion concentrations (Trafford *et al.* 1995; Ottolia *et al.* 2009); it is expressed as follows:

$$I_{\text{NCX}} = \frac{\text{NCX}_{\text{max}}}{1 + K_{\text{ncx}}/\text{Ca}} \quad (10)$$

where the  $\text{Ca}^{2+}$ -dissociation constant and maximal turnover rate are denoted  $K_{\text{ncx}}$  and  $\text{NCX}_{\text{max}}$ , respectively.  $K_{\text{ncx}}$  is estimated to be around 3.6  $\mu\text{M}$  (e.g. Weber *et al.* 2001). This value indicates that NCX responds to  $\text{Ca}^{2+}$  in T-space dynamically, without saturation. For forward model simulations,  $\text{NCX}_{\text{max}}$  and  $K_{\text{ncx}}$  in eqn

(10) were determined by best fit to data simulated using eqn (1) in Weber *et al.* 2001 (Supplemental Fig. S3A).  $\text{NCX}_{\text{max}}$  and  $K_{\text{ncx}}$  depend on  $V$  and intracellular sodium concentration ( $\text{Na}_i$ ), respectively. Our simulation shows that  $K_{\text{ncx}}$  increases from 3 to 11  $\mu\text{M}$  as  $\text{Na}_i$  increases from 4 to 16 mM (Supplemental Fig. S3B) and is not sensitive to  $V$  in the range from  $-90$  to  $-50$  mV.  $\text{NCX}_{\text{max}}$  magnitude decreases from 7.5 to 5  $\mu\text{A } \mu\text{F}^{-1}$  when  $V$  increases from  $-90$  to  $-50$  mV (Supplemental Fig. S3C) and is not sensitive to  $\text{Na}_i$  in the range from 4 to 16 mM.

Unlike the original formulation (Weber *et al.* 2001), eqn (10) can be readily inverted to calculate  $\text{Ca}^{2+}$  in terms of  $I_{\text{NCX}}$ , as required for inverse  $\text{Ca}^{2+}$  estimation. Assuming that total  $I_{\text{NCX}}$  is the sum of two populations (in T-space and M-space), eqn (10) is represented as follows:

$$I_{\text{NCX}} = \text{NCX}_{\text{max}} \left( \frac{1 - \beta}{1 + K_{\text{ncx}}/\text{Ca}_m} + \frac{\beta}{1 + K_{\text{ncx}}/\text{Ca}_t} \right) \quad (11)$$

where  $\beta$  is the fraction of  $I_{\text{NCX}}$  in the T-space (sensing  $\text{Ca}_t$ ). Manipulating eqn (11) leads to the following expression

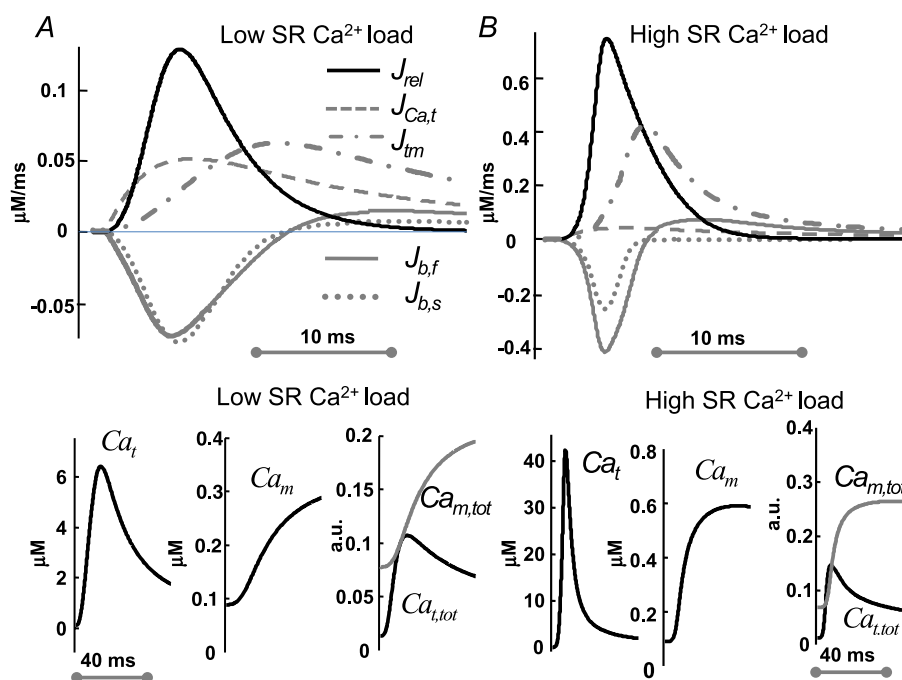


**Figure 3. The relative contributions of different  $\text{Ca}^{2+}$  fluxes to  $\text{Ca}_t$  is SR-load dependent**

The time course of  $\text{Ca}^{2+}$  fluxes in the T-space (top) and  $\text{Ca}^{2+}$  redistribution between  $\text{Ca}_t$  and  $\text{Ca}_m$  (bottom) as a function of  $J_{\text{rel}}$  (SR  $\text{Ca}^{2+}$  load). Top:  $J_{\text{rel}}$  (black trace), trans-sarcolemmal  $\text{Ca}^{2+}$  influx,  $J_{\text{Ca},t}$  (dashed grey trace),  $\text{Ca}^{2+}$  efflux from T-space to M-space,  $J_{\text{tm}}$  (grey dashed-dot trace) and fast ( $J_{\text{b},f}$ , continuous grey trace) and slow ( $J_{\text{b},s}$ , dotted grey trace) buffering fluxes. Bottom (left to right): corresponding free  $\text{Ca}_t$ , free  $\text{Ca}_m$  and total (free and buffered)  $\text{Ca}^{2+}$  content in M-space ( $\text{Ca}_{m,\text{tot}}$ , grey) and T-space ( $\text{Ca}_{t,\text{tot}}$ , black) as fractions of the total cell  $\text{Ca}^{2+}$  content. A, at low SR  $\text{Ca}^{2+}$  load,  $\text{Ca}_i = \text{Ca}_n = 0.875$  (small  $J_{\text{rel}}$ ). B, at a large SR  $\text{Ca}^{2+}$  load,  $\text{Ca}_i = \text{Ca}_n = 1.167$  mM (large  $J_{\text{rel}}$ ). Note that panels A and B use different scales and  $J_{\text{rel}}$  is normalized by  $v_{\text{jt}}$  (eqn (1)).

for  $\overline{Ca_t}$ :

$$\overline{Ca_t} = \frac{K_{NCX}}{\beta} \frac{1}{I_{NCX}/NCX_{max} - (1 - \beta)/(1 + K_{NCX}/Ca_m)} - 1 \quad (12)$$

The value of  $\beta$  can be estimated directly using immuno-histochemical methods. Here, the parameter  $\beta$  was determined from the best fit of simulated  $Ca_m$  and  $I_{NCX}$  to those measured experimentally using the caffeine induced  $J_{rel}$  protocol.  $NCX_{max}$  was calibrated during the phase of  $Ca_m$  when both  $I_{NCX}$  populations sense the same  $Ca^{2+}$  (i.e.  $Ca_t = Ca_m$ ) and eqn (11) reduces to eqn (10). Time to equilibrium of  $Ca_t$  with  $Ca_m$  was estimated using model simulations.

**$Ca_t$  estimation using  $I_{NCX}$  and  $Ca_m$ :  $Ca_t$  estimation using  $I_{NCX}$  and  $Ca_m$  during  $J_{rel}$  induced by a caffeine pulse.** A commonly used intervention to study  $I_{NCX}$  activity is the caffeine pulse experiment, where rapid application of caffeine depletes the SR  $Ca^{2+}$  content and produces a  $Ca_m$  rise that activates  $I_{NCX}$  (e.g. Trafford *et al.* 1995). We simulated the application of caffeine by increasing the sensitivity of  $J_{rel}$  to  $Ca_t$ , reducing its refractoriness and decreasing its regulation by SR  $Ca^{2+}$  eqn (A2) in Appendix) (Kong *et al.* 2008). In addition, SERCA activity was inhibited (Blinks *et al.* 1972). The time course of caffeine-induced  $J_{rel}$  and consequently of  $Ca_m$  and  $I_{NCX}$  were different from those induced by voltage and  $I_{Ca}$ . During caffeine induced  $J_{rel}$ , both the J-space and N-space  $Ca^{2+}$  pools were depleted. Taking advantage of the fully controlled *in silico* conditions, we utilized a  $J_{rel}$ -clamp protocol to simulate caffeine application; the  $J_{rel}$  waveform was represented by a Gaussian function,  $J_{rel} = A \exp[-(t - \mu)^2/\sigma]$ , where the parameters  $A$ ,  $\mu$ , and  $\sigma$  were fitted to match the  $I_{NCX}$  and  $Ca_m$  measured in the experiment, while keeping the total amount of  $Ca^{2+}$  released ( $\int J_{rel} dt$ ) constant and equal to the initial total SR  $Ca^{2+}$  content.

**$Ca_t$  estimation using  $I_{NCX}$  and  $Ca_m$ :  $Ca_t$  estimation using  $I_{NCX}$  tail current and  $Ca_m$ .** We also simulated an  $I_{NCX}$ -tail current experiment, which activates  $J_{rel}$  by the CICR mechanism via  $I_{Ca}$  (Egan *et al.* 1989). Square depolarizing pulses were applied from holding ( $V_h$ ) to depolarizing ( $V_d$ ) potentials to ensure cell-wide  $J_{rel}$ . The  $I_{NCX}$  tail current, measured a few milliseconds after return to  $V_h$ , allows for separation of  $I_{NCX}$  from all other  $Na^+$ - and  $Ca^{2+}$ -dependent currents, which inactivate very rapidly at negative voltages ( $V_h$ ) and do not contribute significantly to the total current. Optically assessed  $Ca_m$  was sampled simultaneously. This procedure was repeated with a progressively increased duration of depolarizing pulses (with increments of  $\Delta t$  ms), which were allowed to

cover the entire duration of the  $Ca^{2+}$  transient elicited by  $J_{rel}$ . The values of the  $I_{NCX}$  and  $Ca_m$  were used as input to eqn (12). This method relies on the assumption that  $J_{rel}$  is independent of the depolarizing pulse duration.

## Results

### Relative contributions of $Ca^{2+}$ fluxes to $Ca_t$ are SR-load dependent

Model simulations were conducted to test the assumptions made with regard to contributions of different  $Ca^{2+}$  fluxes to the time course of  $Ca_t$ . The top panels in Fig. 3 show the time course of  $Ca^{2+}$  fluxes in T-space during depolarization to 10 mV for 200 ms, for a small (Fig. 3A) or large (Fig. 3B)  $J_{rel}$  (note that  $J_{rel}$  in Fig. 3 is normalized by  $v_{jt}$ ; eqn (1)).  $Ca^{2+}$  contribution to  $Ca_t$  from trans-sarcolemmal  $Ca^{2+}$  flux into the T-space,  $J_{Ca,t}$  (dominated by  $I_{Ca}$ , dashed grey) is almost 50% that of  $J_{rel}$  (black trace) when  $J_{rel}$  is small (due to a small SR  $Ca^{2+}$  load,  $Ca_j = Ca_n = 0.875$  mM). In contrast, the contribution from  $J_{Ca,t}$  is negligible when  $J_{rel}$  is large (large SR  $Ca^{2+}$  load,  $Ca_j = Ca_n = 1.167$  mM). This verifies that  $J_{rel}$  is a good surrogate for  $Ca_t$  at larger SR  $Ca^{2+}$  loads. The time course of  $Ca^{2+}$  in the J-space and N-space is shown in Supplemental Fig. S2. Note that small changes in  $Ca_j$  result in large changes of  $J_{rel}$ .  $J_{rel}$  lags slightly behind  $J_{Ca,t}$ , reflecting the typical CICR sequence. Contributions of the fast ( $J_{b,f}$  dotted grey) and slow ( $J_{b,s}$  continuous grey) buffers are also  $J_{rel}$  dependent. The relative contribution of  $J_{b,f}$  increases with increased  $J_{rel}$ . Note that initially  $J_{b,f}$  and  $J_{b,s}$  act as  $Ca^{2+}$  sinks (negative fluxes), decreasing  $Ca_t$ ; later, the buffering fluxes reverse direction, increasing  $Ca_t$ . The buffering fluxes reverse direction earlier (by 5 ms) when  $J_{rel}$  is large. The peak of the  $Ca^{2+}$  flux from T-space to M-space ( $J_{tm}$ , dashed-dot grey curve) coincides with the reversal of the buffering fluxes, demonstrating the importance of including  $Ca^{2+}$  buffering sites in the model.

### Magnitude and time course of $Ca_t$ and $Ca_m$ are different and SR load dependent

The bottom panels in Fig. 3A show, for small  $J_{rel}$  (small SR  $Ca^{2+}$  load),  $Ca_t$ ,  $Ca_m$  and the total  $Ca^{2+}$  content (free and bound) in M-space ( $Ca_{m,tot} = Ca_m + Ca_{trpn} + Ca_{cmdn}$ , grey) and T-space ( $Ca_{t,tot} = Ca_t + Ca_{b,f} + Ca_{b,s}$ , black), normalized by the total cell  $Ca^{2+}$  content. Figure 3B shows similar data, but for a large  $J_{rel}$  (large SR  $Ca^{2+}$  load). Importantly, the results show that even  $Ca^{2+}$  flux via  $I_{Ca}$  alone has sufficient capacity to increase  $Ca_t$  up to  $\sim 5 \mu M$  and thus to induce inactivation of LCCs in T-space. LCCs in M-space are exposed to smaller  $Ca^{2+}$  values and

the relative contribution of CDI to their inactivation is smaller.

The time course of  $Ca_{m,tot}$  and  $Ca_{t,tot}$  indicates that the total amount of  $Ca^{2+}$  in the T-space can reach similar values to those in the M-space for a brief period of time, during both small and large  $J_{rel}$ , in spite of a large ( $\sim 70$  fold) difference in the compartments' volumes. This indicates that buffering capacitance is more important in determining the balance of  $Ca^{2+}$  fluxes during dynamic  $Ca^{2+}$  transients than the compartmental volumes *per se*.

### Partition of NCX between T-space and M-space

To investigate the effect of  $I_{NCX}$  localization on  $Ca_i$  and to estimate the fraction of NCX in T-space ( $\beta$ ), we simulated a caffeine pulse protocol and compared the results to experimental data. The amplitude of the simulated caffeine-induced intracellular calcium transient agrees well with the measurements (compare Fig. 4A right and left panels).

The left panels in Fig. 4 show experimentally recorded  $Ca^{2+}$  transient ( $Ca_m$ ) (Fig. 4A) and  $I_{NCX}$  (Fig. 4B) after caffeine induced  $J_{rel}$ . A phase plot of  $I_{NCX}$  vs.  $Ca_m$  is provided in Fig. 4C (same data as in Fig. 4A and Fig. 4B).  $I_{NCX}$  is a bi-valued function of  $Ca_m$ ; that is, one value of  $Ca_m$  (e.g.  $c_1$ ) is associated with two values of  $I_{NCX}$  ( $\alpha_1$  and  $\alpha_2$ ). Figure 4D shows that  $I_{NCX}$  precedes global  $Ca_m$  by 25 ms. The right panels in Fig. 4 show the corresponding simulated  $Ca_m$  (Fig. 4A) and  $I_{NCX}$  (Fig. 4B) as a function of  $I_{NCX}$  fractional population in T-space,  $\beta$  (arrow in Fig. 4B indicates increasing  $\beta$ ). The corresponding simulated phase plots of  $I_{NCX}$  vs.  $Ca_m$  are shown in Fig. 4C (right). As in the experiment,  $I_{NCX}$  is a bi-valued function of  $Ca_m$ ; for example  $Ca_m = 0.4 \mu M$  ( $c_1$ ) is associated with two values of  $I_{NCX}$  ( $\alpha_1 = -1 \mu A \mu F^{-1}$  and  $\alpha_2 = -2.3 \mu A \mu F^{-1}$ ). Note that for  $\beta = 0$  (all  $I_{NCX}$  in M-space),  $I_{NCX}$  is a single-valued function of  $Ca_m$  (dashed grey trace). Thus, the hysteresis and delay between the peaks of  $Ca_m$  and  $I_{NCX}$  are due to the existence of a population of  $I_{NCX}$  that senses  $Ca_t$ , which rises faster and reaches higher values than the cell-average  $Ca^{2+}$ . The area of the hysteresis loop was

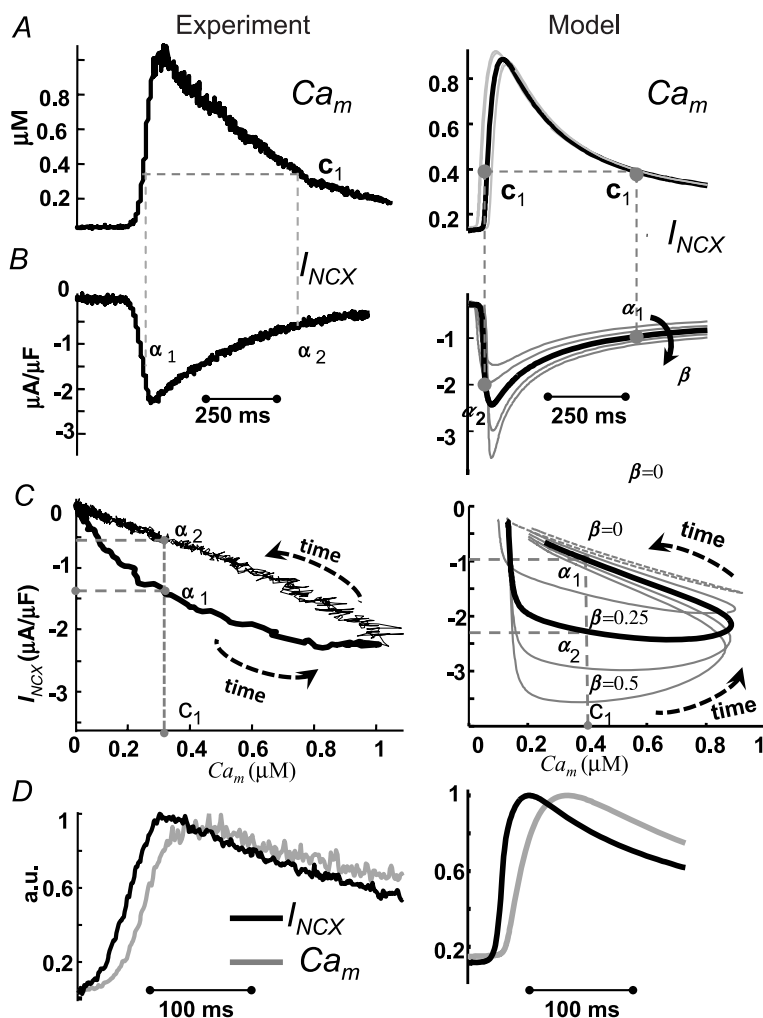


**Figure 4. An NCX partition of 25% in T-space and 75% in M-space provides the best fit to experimental data**

Peak  $Ca_m$  lags by 25 ms relative to peak  $I_{NCX}$ , reflecting the NCX partition. The fraction of NCX in T-space,  $\beta$  (right panels), estimated from best fit to experimental data (left panels). Experimentally recorded  $Ca_m$  (A, left) and  $I_{NCX}$  (B, left) evoked by caffeine pulse;  $V$  was held at  $-80$  mV. Phase plots of  $I_{NCX}$  vs.  $Ca_m$  are constructed in C from the data in A and B. It is clear from panel C that  $I_{NCX}$  is a bi-valued function of  $Ca_m$ ; that is, one value of  $Ca_m$  (e.g.  $c_1$ ) is associated with two values on  $I_{NCX}$  ( $\alpha_1$  and  $\alpha_2$ ). In panel C, right,  $\beta$  (fraction of NCX in T-space) is varied from 0 to 0.5. The continuous black trace is for 25% of  $I_{NCX}$  ( $\beta = 0.25$ ) in the T-space, which provides the best fit for the experimental data. Note that for  $\beta = 0$  (grey dashed trace),  $I_{NCX}$  is a single-valued function of  $Ca_m$ . D,  $I_{NCX}$  (black) and  $Ca_m$  (grey), corresponding to the traces in panels A and B, are shown on an expanded time scale.  $Ca_m$ , normalized to its peak value, is superimposed on normalized and inverted  $I_{NCX}$ . Note that peak  $I_{NCX}$  precedes peak  $Ca_m$  by about 25 ms in both simulation and experiment.



chosen as a criterion for determining the best fit to experimental data; it reflects the difference between the ascending (due to increase of  $Ca_m$ ) and descending (due to decrease of  $Ca_m$ ) limbs of the  $I_{NCX}$  curves and the relative contribution of  $Ca_t$  to whole-cell  $I_{NCX}$ . The continuous black curve is for  $\beta = 0.25$ ; it provides the best fit for the experimental data and a similar delay (Fig. 4D) to that measured experimentally. Based on this fit, all estimations of  $Ca_t$  were conducted for 25%  $I_{NCX}$  in T-space (75% in M-space;  $\beta = 0.25$ ).

### Estimation of $Ca_t$ using $I_{NCX}$ and $Ca_m$ due to caffeine induced $J_{rel}$

Figure 5 shows estimation of  $Ca_t$  ( $\overline{Ca_t}$ ) during a caffeine pulse experiment similar to that in Fig. 4, but from a different cell.  $V$  was held constant throughout at  $-70$  mV. The top panels in Fig. 5 show experimentally recorded  $Ca_m$  (Fig. 5A) and  $I_{NCX}$  (Fig. 5B) after caffeine induced  $J_{rel}$ . A phase plot of  $I_{NCX}$  vs.  $Ca_m$  is provided in Fig. 5C (same data as in Fig. 5A and Fig. 5B). Figure 5D shows measured  $Ca_m$  (grey trace) and inverse-estimated  $\overline{Ca_t}$  (black trace) using  $Ca_m$  and  $I_{NCX}$  as input to eqn (12).  $Na^+$ -sensitive

$K_{NCX}$  was set to  $3.6$  mM and  $NCX_{max}$  was estimated to be  $11 \mu A \mu F^{-1}$ . These results predict a peak  $Ca_t$  in the range of  $10 \mu M$ , with time to equilibrium with global  $Ca_m$  of  $250$ – $350$  ms. The  $Ca_t$  peak value is an order of magnitude larger than global  $Ca_m$  ( $1 \mu M$ ).

The bottom panels of Fig. 5 show model-generated data. As explained in Methods, a  $J_{rel}$ -clamp protocol was used (waveform in inset to panel A). The duration of  $J_{rel}$  was set so that the time course of  $Ca_t$  estimated using experimental data matched that of  $Ca_t$  generated by the model. The best fit was achieved with  $J_{rel} = 400 \exp[-(t - 45)^2/200]$ . Model generated  $Ca_t$  (black) and  $Ca_m$  (dashed grey) are shown in Fig. 5D, bottom; both are very similar to experimental  $Ca_m$  and  $\overline{Ca_t}$  (Fig. 5D, top). The model predicts that the time course of  $Ca_m$  and  $I_{NCX}$  during caffeine-pulse experiment is  $V$  dependent (Supplemental Fig. S4). Peak  $Ca_m$  (Supplemental Fig. S4A) increases and peak  $I_{NCX}$  decreases (Supplemental Fig. S4A) with depolarizing voltage. Time to equilibrium between  $Ca_t$  and  $Ca_m$  shows a moderate  $V$ -dependence (Supplemental Fig. S4D); it is shorter for negative  $V$ . This is important, because to calibrate  $NCX_{max}$ ,  $Ca_m$  and  $Ca_t$  should reach equilibrium.

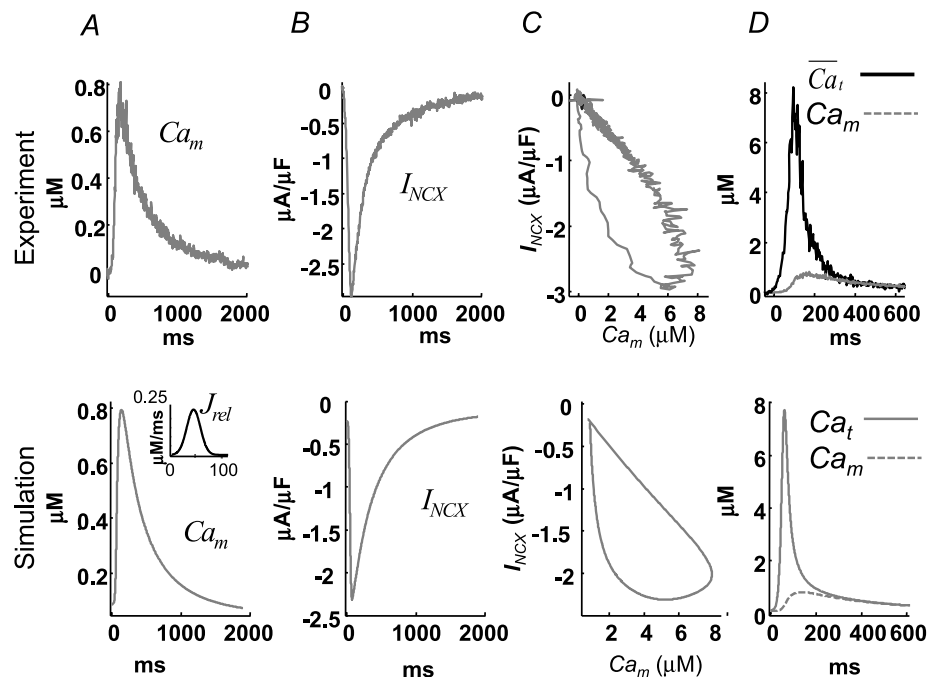


**Figure 5.** The time course of  $Ca_t$  can be estimated from caffeine-induced  $I_{NCX}$  and  $Ca_m$ ; it shows different dynamics from  $Ca_t$  generated by CICR

Experimentally recorded  $Ca_m$  (A, top) and  $I_{NCX}$  (B, top) evoked by a caffeine pulse;  $V$  was held at  $-70$  mV. Phase plots of  $I_{NCX}$  vs.  $Ca_m$  are constructed in C from the data in A and B. D, estimated  $Ca_t$ ,  $\overline{Ca_t}$ , using eqn (12) with  $I_{NCX}$  from A and  $Ca_m$  from B as input. For the model-generated data (bottom panels), the  $J_{rel}$  waveform shown in the inset to panel A, bottom, was used as input. Model generated (D, bottom)  $Ca_t$  (black) and  $Ca_m$  (grey) are shown for comparison with those estimated from experimental data (D, top).

### Ca<sub>t</sub> estimation using $I_{\text{NCX}}$ tail current and Ca<sub>m</sub> due to CICR

Figure 6 shows experimental (top) and simulated (bottom) results of the  $I_{\text{NCX}}$  tail current protocol. During the simulations, similar to experimental protocols,  $V$  pulses were applied from a holding ( $-70$  mV) to a depolarizing ( $10$  mV) potential. The depolarizing step was interrupted at different time intervals (increments of  $10$  ms in the experiment), stepping back to  $-70$  mV (see inset in Fig. 6A). In the simulations (bottom panels of Fig. 6), the time increments were decreased to  $5$  ms in order to increase sampling and thus the quality of the estimation; traces for the first and last  $V$  pulses are shown as continuous and dashed black lines, respectively. In Fig. 6A changes of  $I_{\text{NCX}}$  tail current amplitude with pulse duration (circles) reflect changes of Ca<sub>t</sub> sensed by  $I_{\text{NCX}}$ . Corresponding values of Ca<sub>m</sub> were sampled at the same time and are indicated by circles in Fig. 6B; note that the locus of sampled Ca<sub>m</sub> values coincides with the Ca<sub>m</sub> transient during the last (dashed black) pulse. This indicates that the same  $J_{\text{rel}}$  (and consequently Ca<sub>t</sub>) is evoked by each pulse, ensuring that the estimation of  $\overline{\text{Ca}}_t$  is unique.

Figure 6C shows estimated  $\overline{\text{Ca}}_t$  from experimental (top) and model generated (bottom)  $I_{\text{NCX}}$  and Ca<sub>m</sub> data. In the bottom panel, the actual model-computed Ca<sub>t</sub> traces (grey) are also shown as a gold standard for comparison. Importantly, the  $I_{\text{NCX}}$ -based method is able to recover both the ascending and descending limbs of Ca<sub>t</sub>. However, it is difficult to estimate the value of peak Ca<sub>t</sub> using this method with sufficient accuracy due to the limited number of sampling points, which limits its temporal resolution.

Note that the first three model simulated  $I_{\text{NCX}}$  tail current traces (bottom of Fig. 6A) are biphasic (increasing then decreasing in magnitude) and reach their peaks after the end of the  $V$  pulse. This non-monotonic behaviour is because Ca<sub>t</sub> is still increasing during the first  $30$  ms of simulation (Fig. 6C). This early phase was not covered by the experimental protocol (top of Fig. 6A). Note that  $I_{\text{NCX}}$  reaches its maximum negative magnitude earlier than peak Ca<sub>m</sub>, reflecting the existence of a T-space population of  $I_{\text{NCX}}$  which is activated by Ca<sub>t</sub>. Ca<sub>m</sub> reaches its peak value at  $50$  ms,  $25$  ms later than  $I_{\text{NCX}}$  (arrows in Fig. 6A and B), which corresponds well to the results of the caffeine pulse simulations in Fig. 4D.

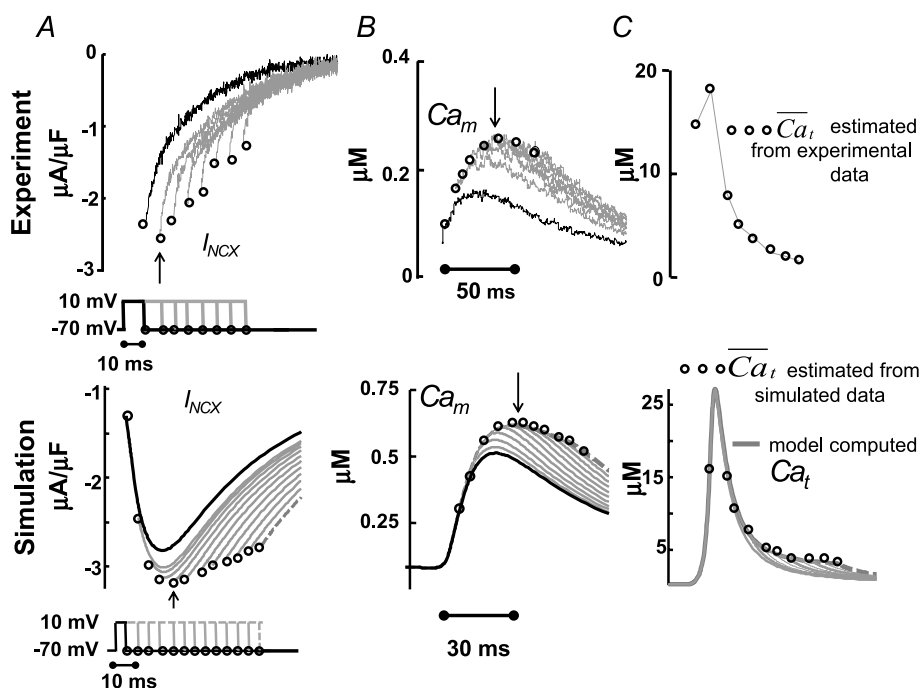


**Figure 6. The time course of Ca<sub>t</sub>, estimated from the  $I_{\text{NCX}}$  tail current**

Estimation of free Ca<sup>2+</sup> in T-space, Ca<sub>t</sub>, using experimentally measured (top) and model generated (bottom)  $I_{\text{NCX}}$  and Ca<sub>m</sub>, generated by  $V$  pulses as shown in the inset. A,  $I_{\text{NCX}}$  tail current traces. Raw current traces were truncated before the voltage was returned to the holding potential. Simulated traces, corresponding to the first and last  $V$  pulses, are shown in continuous and dashed black lines, respectively. B, corresponding optically measured (top) or model simulated (bottom) Ca<sub>m</sub>. Circles in panels A and B indicate peaks of  $I_{\text{NCX}}$  tail currents and corresponding Ca<sub>m</sub> values. Arrows in A and B indicate peak  $I_{\text{NCX}}$  and Ca<sub>m</sub>, respectively. C, estimated Ca<sub>t</sub>,  $\overline{\text{Ca}}_t$ , using eqn (12) with  $I_{\text{NCX}}$  from A and Ca<sub>m</sub> from B as input. For the model-generated data (bottom panel), the actual model computed Ca<sub>t</sub> is shown (grey traces) together with the estimated  $\overline{\text{Ca}}_t$  (circles).

### Estimation of $\overline{Ca_t}$ using $I_{Ca}$ inactivation as reporter ( $\Delta I_{Ca}$ -based method)

**Model-based validation of the  $\Delta I_{Ca}$  method.** To elucidate the effect of the normalization procedure in eqn (9) on  $\overline{Ca_t}$ , we simulated  $V$  and  $Ca_t$  clamp protocols in Fig. 7. The model cell was depolarized to 10 mV for 200 ms (Fig. 7A top, inset) and  $Ca_t$  was also clamped to 20  $\mu M$  for 20 ms, with a progressive 5 ms shift of  $Ca_t$  pulse onset (Fig. 7A bottom, inset) as indicated by arrow. Figure 7A shows five  $I_{Ca}$  traces elicited by the  $V$  step, with four  $Ca_t$  pulses following the  $I_{Ca}$  descending limb. The first  $I_{Ca}$  trace ( $I_{Ca}^0$ , blue dashed curve) was simulated without applying a  $Ca_t$  pulse, and thus shows inactivation by only a  $V$ -dependent mechanism. Figure 7B shows the difference current  $\Delta I_{Ca} = I_{Ca} - I_{Ca}^0$ ; note that peak  $\Delta I_{Ca}$  is progressively decreased as  $Ca_t$  pulses are progressively delayed relative to the  $V$  pulse (circles in Fig. 7B). This indicates that the contribution of  $Ca_t$  to  $I_{Ca}$  inactivation decreases with the delay, despite the identical waveforms of  $Ca_t$  pulses. Consequently, calibration of  $\Delta I_{Ca}$  by peak  $I_{Ca}^0$  results in the  $\overline{Ca_t}$  shown in Fig. 7C, which is progressively underestimated as the onset of the  $Ca_t$  pulse is increasingly delayed relative to the onset of the  $V$  step. This is because  $I_{Ca}$  is subjected to  $V$ -dependent inactivation immediately after onset of the depolarizing pulse; the longer delay between the  $V$  and  $Ca_t$  pulses results in greater  $I_{Ca}$  inactivation by VDI (not CDI, which is the basis of the  $\Delta I_{Ca}$  method), smaller  $\Delta I_{Ca}$ , and consequently a smaller estimate of  $\overline{Ca_t}$ . To correct for this artifact of pulse delay, we calibrated each  $\Delta I_{Ca}$  trace by  $I_{Ca}^0$  values at the time when  $\Delta I_{Ca}$  was maximal (i.e. contribution of  $Ca_t$  to  $I_{Ca}$  inactivation was maximal). The resulting  $\overline{Ca_t}$  traces are shown in Fig. 7D; note that with this calibration, the peaks

of  $\overline{Ca_t}$  are identical (time-invariant), independent of the  $Ca_t$  pulse time delay.

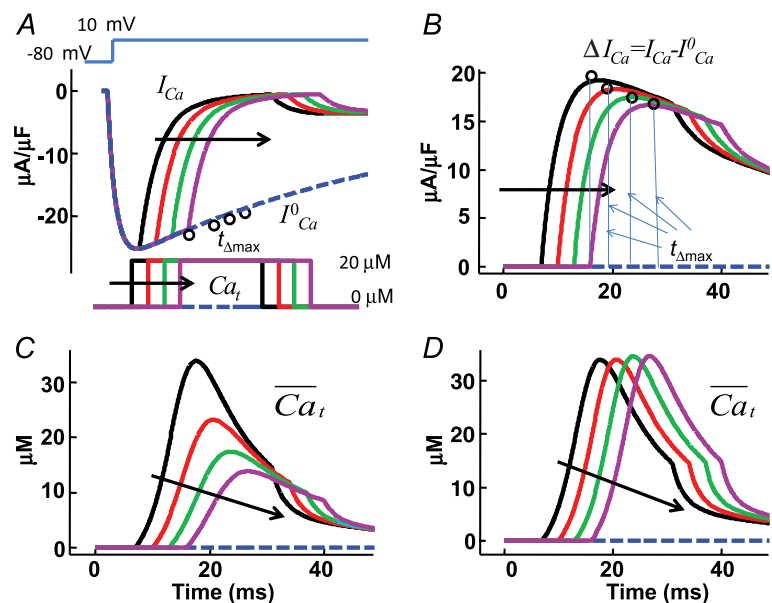
**Estimation of  $\overline{Ca_t}$  from experimental data and comparison to model simulation.** Figure 8 shows estimation of  $\overline{Ca_t}$  by the  $\Delta I_{Ca}$ -based method, using experimental (top panels) and model simulated (bottom panels) data. The experimental data set was from a different cell from the one in Fig. 2; however the  $V$ -clamp protocol was identical (inset in Fig. 2). Both experimental and simulated  $I_{Ca}$  show similar dependence on  $J_{rel}$ . That is, both peak amplitude and residual current decrease as  $J_{rel}$  increases. In Fig. 8A the current trace evoked by the first pulse after SR depletion by caffeine is denoted by  $I_{Ca}^0$  (black trace).  $J_{rel}$  significantly inactivates and decreases  $I_{Ca}$  immediately ( $\sim 2$  ms) after  $J_{rel}$  initiation, while maximal inactivation of  $I_{Ca}$  is reached after 5–10 ms. The model data were generated using graded initial values of  $Ca_i = Ca_n$  from 0 to 1.5 mM.

Figure 8B shows the difference current  $\Delta I_{Ca} = I_{Ca} - I_{Ca}^0$ . The traces exhibit a biphasic behaviour, with a fast initial increase reaching a maximum at around 10 ms, followed by a slow decrease which lasts for more than 60 ms. Model-based analysis of these data clarifies that the first phase of  $\Delta I_{Ca}$  is dominated by an increase of  $Ca_t$  due to  $J_{rel}$ , while the second phase is dominated by  $Ca^{2+}$  diffusion from T-space to M-space,  $J_{tm}$ .

Figure 8C shows estimated  $\overline{f_{Ca}}$  using experimental (top) and simulated (bottom, dashed black) data as input to eqn (9). Circles in Fig. 8A and B indicate  $I_{Ca}^0$  at  $t_{\Delta max}$  and maximal  $\Delta I_{Ca}$ , respectively. Model computed  $\overline{f_{Ca}}$  traces (continuous grey) are shown in Fig. 8C as a gold standard for comparison. The trace of  $\overline{f_{Ca}}$  which corresponds to

**Figure 7. Model-based validation of the  $\Delta I_{Ca}$  method for estimating  $\overline{Ca_t}$**

A, model simulated traces of  $I_{Ca}$  evoked by a depolarizing step to 10 mV (inset on top) in the presence of controlled (calcium clamp)  $Ca_t$  pulses of 20  $\mu M$  amplitude and 25 ms duration, with progressively delayed onset by 5 ms (arrows; inset on bottom).  $I_{Ca}^0$ , blue dashed trace, is subjected to  $V$ -dependent inactivation only ( $Ca_t$  set to zero). Circles indicate the values of  $I_{Ca}^0$  at time  $t_{\Delta max}$ . Note that all traces coincide prior to application of the  $Ca_t$  pulse. B, difference current,  $\Delta I_{Ca} = I_{Ca} - I_{Ca}^0$ . Circles indicate the maximal values of  $\Delta I_{Ca}$ , occurring at time  $t_{\Delta max}$ . C,  $\overline{Ca_t}$  estimated with  $\Delta I_{Ca}$  normalized by peak  $I_{Ca}^0$  (old method). D,  $\overline{Ca_t}$  estimated by normalizing each  $\Delta I_{Ca}$  trace by the corresponding value of  $I_{Ca}^0$  at time  $t_{\Delta max}$  (eqn (8); new method).



CDI in the absence of RDI ( $J_{\text{rel}} = 0$ ) is denoted by a square symbol. Note that the  $\bar{f}_{\text{Ca}}$  trace which corresponds to  $I_{\text{Ca}}^0$  (indicated by a star) is equal to unity, i.e. it predicts correctly the absence of  $I_{\text{Ca}}$  inactivation due to RDI. In contrast, the model computed  $f_{\text{Ca}}$  trace, indicated by a square, is different from unity. Unlike  $\bar{f}_{\text{Ca}}$ , which is estimated via RDI (due to  $J_{\text{rel}}$  only),  $f_{\text{Ca}}$  accounts for CDI due to all  $\text{Ca}^{2+}$  fluxes into the T-space. Fluxes other than  $J_{\text{rel}}$  (via LCC and NCX) contribute to CDI (compare traces indicated by square and star symbols). Clearly,  $\bar{f}_{\text{Ca}}$  underestimates CDI of  $I_{\text{Ca}}$  because it does not consider  $\text{Ca}^{2+}$  fluxes other than  $J_{\text{rel}}$ . However, as SR load increases (arrow),  $J_{\text{rel}}$  increases and the accuracy of  $\bar{f}_{\text{Ca}}$  estimation improves, especially during the descending limb of  $f_{\text{Ca}}$ . Figure 8D shows  $\bar{\text{Ca}}_{\text{t}}$  (dashed black traces) estimated using  $\bar{f}_{\text{Ca}}$  as an input to eqn (8) (top panel is from experimental data; bottom panel from model generated data). In addition, Fig. 8D (bottom) shows the actual

model computed  $\text{Ca}_{\text{t}}$  (grey traces) for comparison. Note that the  $\bar{\text{Ca}}_{\text{t}}$  trace which corresponds to  $I_{\text{Ca}}^0$  (star) is equal to zero (depleted SR,  $J_{\text{rel}} = 0$ ), while the corresponding  $\text{Ca}_{\text{t}}$  (square) is not (it reaches peak values of 2–3  $\mu\text{M}$ ) due to contribution from LCC and reverse-mode NCX. As SR load increases,  $J_{\text{rel}}$  increases and the accuracy of  $\bar{\text{Ca}}_{\text{t}}$  estimation (assessed as the ratio of peak  $\text{Ca}_{\text{t}}$  to peak  $\bar{\text{Ca}}_{\text{t}}$ ) improves. This is due to an increased contribution of  $J_{\text{rel}}$ -dependent RDI to total CDI. Using normalized peak differences of the corresponding  $\text{Ca}_{\text{t}}$  and  $\bar{\text{Ca}}_{\text{t}}$  in Fig. 8D (bottom), the estimation error decreases from 47% to 7% as SR load increases.

The ascending phase of  $\text{Ca}_{\text{t}}$  is estimated with a greater accuracy than the descending phase. This is because the method is based on the  $J_{\text{rel}}$  component of inactivation and peak  $J_{\text{rel}}$  coincides with the steepest ascending portion of  $\text{Ca}_{\text{t}}$ . In addition, a large  $J_{\text{rel}}$  accelerates inactivation, which makes the instantaneous approximation between  $\text{Ca}_{\text{t}}$

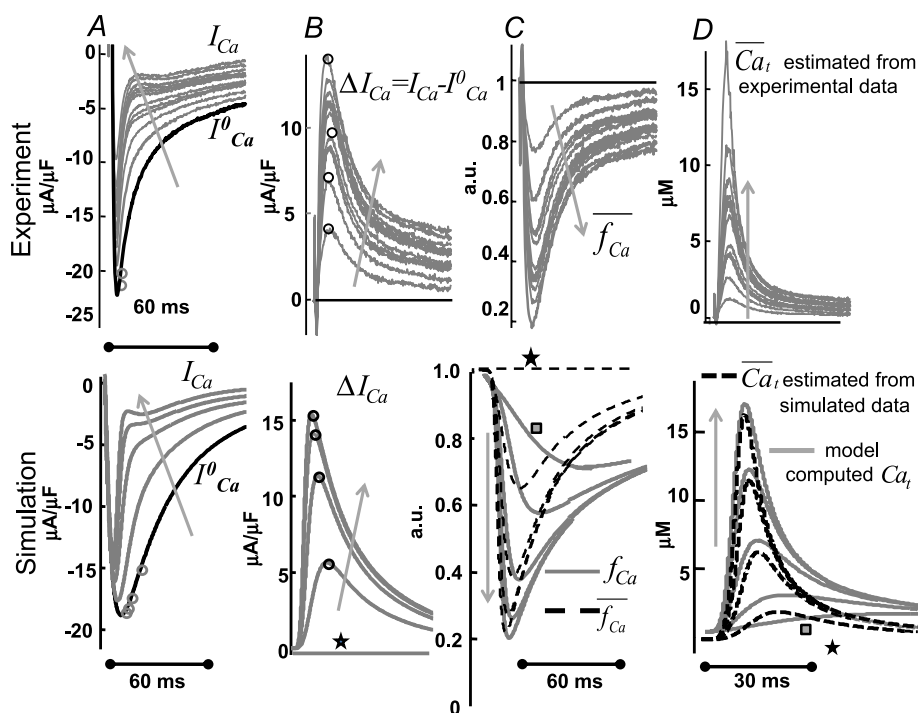


**Figure 8. Estimation of  $\text{Ca}_{\text{t}}$  from  $J_{\text{rel}}$ -dependent inactivation of  $I_{\text{Ca}}$  using the  $\Delta I_{\text{Ca}}$  method**

Estimation of free  $\text{Ca}^{2+}$  in T-space ( $\bar{\text{Ca}}_{\text{t}}$ ) using experimentally measured (top) and model simulated (bottom)  $I_{\text{Ca}}$ . A, superimposed traces of  $I_{\text{Ca}}$  evoked by depolarizing pulses to 10 mV (V-clamp protocol is identical to that in the inset of Fig. 2); levels of SR  $\text{Ca}^{2+}$  load increase with the number pulses (arrows).  $I_{\text{Ca}}^0$  is the current trace evoked by the first pulse after SR depletion by caffeine (black trace). B, difference current,  $\Delta I_{\text{Ca}} = I_{\text{Ca}} - I_{\text{Ca}}^0$ ; the  $\Delta I_{\text{Ca}}$  trace which corresponds to  $I_{\text{Ca}}^0$  (depleted SR;  $J_{\text{rel}} = 0$ ) (continuous black) is equal to zero. Circles indicate the maximal values of  $\Delta I_{\text{Ca}}$ , occurring at time  $t_{\Delta\text{max}}$ . C, estimate of RDI,  $\bar{f}_{\text{Ca}}$ . Each  $\Delta I_{\text{Ca}}$  trace was normalized by the  $I_{\text{Ca}}^0$  value at the time of maximal  $\Delta I_{\text{Ca}}$  ( $t_{\Delta\text{max}}$ , indicated by circles in panel A). In the bottom panel, model computed CDI curves,  $f_{\text{Ca}}$  (grey traces), are also shown for comparison.  $\bar{f}_{\text{Ca}}$  and  $f_{\text{Ca}}$  traces which correspond to  $I_{\text{Ca}}^0$  are indicated by a star and a square, respectively. The  $f_{\text{Ca}}$  trace indicated by a square shows contribution to CDI from  $\text{Ca}^{2+}$  fluxes other than  $J_{\text{rel}}$ . D,  $\bar{\text{Ca}}_{\text{t}}$  estimated via eqn (8) using  $\bar{f}_{\text{Ca}}$  as input. In the bottom panel, model computed  $\text{Ca}_{\text{t}}$  (grey traces) are also shown for comparison.  $\bar{\text{Ca}}_{\text{t}}$  and  $\text{Ca}_{\text{t}}$  traces which correspond to  $I_{\text{Ca}}^0$  are indicated by a star and a square, respectively. The trace indicated by a square shows contribution to  $\text{Ca}_{\text{t}}$  from  $\text{Ca}^{2+}$  fluxes other than  $J_{\text{rel}}$  (via LCC and NCX). Arrows indicate increasing number of depolarizing pulses (SR load).



and inactivation more accurate. However, the  $I_{Ca}$ -based method tends to underestimate the descending portion of  $Ca_t$  when the relative contribution of  $J_{rel}$  to total inactivation is smaller.

## Discussion

In this study, we verified that the minimal model for interactions between  $J_{rel}$ ,  $I_{Ca}$  and  $I_{NCX}$  requires two myoplasmic functional compartments for  $Ca^{2+}$  distribution, T-space and M-space. This compartmental organization differs from the compartmentalization used in previous models (Hund & Rudy, 2004; Shannon *et al.* 2004; Faber *et al.* 2007; Mahajan *et al.* 2008) primarily due to a different partition of LCCs, NCXs and  $Ca^{2+}$  buffers. Inclusion of the T-space, which is structurally associated with RyRs, in the compartmental model of  $Ca^{2+}$  cycling allowed us to reproduce *in silico* the following important experimental results. (1) Hysteresis of  $I_{NCX}$  dependence on  $Ca_m$  during a caffeine application protocol (Fig. 4C). (2) A delay between peak  $I_{NCX}$  and peak  $Ca_m$  during a caffeine application protocol (Fig. 4D). (3) A delay between  $I_{NCX}$  and  $Ca_m$  during CICR (Fig. 6). (4) A rapid  $I_{Ca}$  inactivation ( $\sim 2$  ms) due to  $J_{rel}$ , with a graded inactivation magnitude as a function of the SR  $Ca^{2+}$  content (Fig. 8). (5) A delay between  $I_{Ca}$  inactivation due to  $J_{rel}$  and due to  $Ca_m$  (Fig. 8).

A rapid  $I_{Ca}$  inactivation due to  $J_{rel}$  indicates a strong functional coupling between LCCs and RyRs in ventricular myocytes, which is not surprising because structurally most of the LCCs and RYRs are located in close proximity to each other. NCXs are usually considered to be expressed outside the  $Ca^{2+}$  microdomain of interaction between LCCs and RyRs. However, using the experimental results from the non-failing ventricular myocytes as an input to the compartmental model, we found that a small but significant ( $\sim 25\%$ ) fraction of NCXs is functionally coupled to RyRs via a common pool of  $Ca^{2+}$  ( $Ca_t$ ).

The study provides a theoretical basis for estimating the dynamic properties of  $Ca_t$  using measured  $I_{Ca}$ ,  $I_{NCX}$  and  $Ca_m$  as input to the compartmental model. The model was used to generate  $Ca_t$  transients, simulating specific experimental protocols, and the simulated  $Ca_t$  was used as a gold standard for evaluation of inverse-estimated  $Ca_t$  using  $I_{Ca}$ ,  $Ca_m$  and  $I_{NCX}$ . The simulations confirmed estimations by previous investigators (Egan *et al.* 1989; Trafford *et al.* 1995; Weber *et al.* 2002; Acsai *et al.* 2011), demonstrating that peak  $Ca_t$  is an order of magnitude larger than the corresponding peak  $Ca_m$  and that  $Ca^{2+}$  gradients between T-space and M-space could persist into the late phase of the AP. Previous procedures to estimate  $Ca_t$  from  $Ca^{2+}$ -dependent currents used a reductionist approach by employing each current in isolation. Here we

used data from both  $I_{Ca}$  and  $I_{NCX}$ , where  $J_{rel}$  was induced by either CICR or by caffeine application. The results revealed that the  $I_{Ca}$ -based method is more accurate during the rising phase of  $Ca_t$ , while the  $I_{NCX}$ -based method is more accurate during its slow descending phase. Combined application of both methods provides a close estimate of both phases and a more accurate estimate of the entire  $Ca_t$  than the application of each method alone.

## Characteristics of free $Ca^{2+}$ in T-space ( $Ca_t$ )

The model predicts peak  $Ca_t$  in the range of 6–25  $\mu M$ ; these values are similar to computed  $Ca^{2+}$  transients averaged over many dyadic spaces (15  $\mu M$ , Bondarenko *et al.* 2004; Greenstein *et al.* 2006), but significantly lower than the maximal values computed for a single dyad ( $> 50 \mu M$ , Stern, 1992; Langer & Peskoff, 1998; Higgins *et al.* 2007; Gaur & Rudy, 2011). These results are consistent with our definition of T-space, which assumes a uniform whole-cell  $J_{rel}$  and an average  $Ca_t$  over many dyads. We also found that the time to equilibrium between  $Ca_t$  and  $Ca_m$  was strongly dependent on the experimental conditions, including the amount of  $Ca^{2+}$  released via RyRs (SR  $Ca^{2+}$  load) and the magnitude of the depolarizing  $V$  pulses (the driving force for  $I_{NCX}$ ) (Supplemental Fig. S4). An increase of  $J_{rel}$  and/or of  $V$  increased the time to equilibrium, which was in the range of 50–350 ms, depending on  $J_{rel}$  and  $V$ . The lower bound of these values are consistent with those previously computed in models for CICR (Shannon *et al.* 2004; Greenstein *et al.* 2006; Faber *et al.* 2007). The caffeine pulse protocol shows significant prolongation of  $Ca_t$  duration (Fig. 5).

We found that the time course of  $Ca_t$  is strongly regulated by fast and slow  $Ca^{2+}$  buffers (Fig. 3). We also found that  $J_{rel}$  significantly inactivates and decreases  $I_{Ca}$  immediately ( $\sim 2$  ms) after  $J_{rel}$  initiation, while maximal inactivation of  $I_{Ca}$  due to  $J_{rel}$  is reached after 5–10 ms.

## The compartmental model of $Ca^{2+}$ cycling

The success of inverse  $Ca_t$  estimation depends on the accuracy of the mathematical model used, and how well constrained is the model by experimental data. The model should describe quantitatively the relationship between the time course of  $Ca^{2+}$ -dependent currents and the time course of  $Ca^{2+}$  which modulates them. Below we discuss modelling considerations for  $I_{Ca}$  and  $I_{NCX}$ .

**Accuracy of the  $I_{Ca}$  model.** In the  $I_{Ca}$  model development, we utilized experimental data from porcine ventricular myocytes. Using the Hodgkin–Huxley formalism, model activation and inactivation gates were fitted to reproduce the recorded  $I_{Ca}$   $I$ – $V$  curve (Supplemental Fig. S1). Note that the  $I$ – $V$  curve is SR  $Ca^{2+}$  load dependent (Sham,

1997).  $I_{Ca}$  inactivation was assessed by the conventional two-step voltage-clamp protocol (Stengl *et al.* 2010) (Supplemental Fig. S1). Following (Kass & Sanguinetti, 1984; Lee *et al.* 1985; Hadley & Hume, 1987) we assumed that  $I_{Ca}$  inactivation is  $V$  dependent and is not complete in the absence of  $Ca^{2+}$ . In the model,  $I_{Ca}$  inactivation was characterized by the product of two time-dependent processes: (1) voltage-dependent inactivation modulated by  $Ca^{2+}$ , and (2) a pure free  $Ca^{2+}$ -dependent process.  $Ca^{2+}$ -dependent parameters were fitted to reproduce the magnitude and time course of  $I_{Ca}$  and its dependence on  $J_{rel}$  (variable SR  $Ca^{2+}$  load) (Fig. 2). To validate the model in the context of whole cell  $Ca^{2+}$  cycling, we verified that it reproduces experimentally recorded whole cell  $Ca^{2+}$  transients and  $I_{Ca}$  at different levels of SR  $Ca^{2+}$  load. Model simulated results match simultaneously the experimentally recorded  $I_{Ca}$  (Fig. 2A) and  $Ca_m$  (Fig. 2B) at different levels of  $J_{rel}$  (SR  $Ca^{2+}$  load).

**Accuracy of the  $I_{NCX}$  model.** Bidirectional flux of  $Ca^{2+}$  through NCX depends on  $V$ , intracellular concentration ( $Na_i$ ) and extracellular concentration ( $Na_o$ ) of  $Na^+$  and extracellular concentration of  $Ca^{2+}$  ( $Ca_o$ ), which complicates the analysis. To keep  $I_{NCX}$  operating in the forward ( $Ca^{2+}$  extrusion) mode, experimental protocols were conducted at constant  $V$  close to the resting values ( $\sim -80$  mV) and at low  $Na_i$  ( $< 5$  mM). Since  $Na_o$  and  $Ca_o$  can be controlled in experiments, measured  $I_{NCX}$  can be regarded as a function of  $Ca_m$  and  $Ca_t$  only. An independent measurement of  $Ca_m$  (whole-cell optical signal) allows for a unique estimate of  $Ca_t$ . The formulation proposed by Weber *et al.* (2001) was used as a starting point for  $I_{NCX}$  modelling here. The slow allosteric dependence of  $I_{NCX}$  on intracellular  $Ca^{2+}$  was eliminated based on the recent study of Reeves & Condrescu (2003). We show that the resulting  $I_{NCX}$  model (eqn (10)) can be approximated by a Hill equation with a variable intracellular  $Ca^{2+}$  at fixed  $Na_o$ ,  $Ca_o$ ,  $Na_i$  and  $V$ , conditions that can be realized experimentally. This formulation (eqn (10)) was inverted to calculate  $Ca_t$  in terms of  $I_{NCX}$ , as required for inverse  $\overline{Ca_t}$  estimation (eqn (12)).

### Spatial constraints

In ventricular myocytes,  $Ca^{2+}$  concentration gradients exist between SR dyads, a subsarcolemmal space (including caveolae) and the bulk myoplasm (Trafford *et al.* 1995; Weber *et al.* 2002; Higgins *et al.* 2007). The model used here does not consider the dynamics of  $Ca^{2+}$  in individual dyadic spaces (Shannon *et al.* 2004; Gaur & Rudy, 2011); instead all dyads are incorporated into the T-space and their  $Ca^{2+}$  concentration is assumed to be in rapid equilibrium. This implies that no  $Ca^{2+}$  gradients exist between dyads. Consistently, the experimental

protocols evaluated here rely on the cell-average  $Ca^{2+}$  and are not designed to estimate  $Ca^{2+}$  in a single dyad. Therefore, we implemented protocols for which RyRs are activated uniformly throughout the cell, either by CICR (via LCC flux) or by caffeine-induced- $Ca^{2+}$  release.

### The physical characteristics of T-space

Unlike structurally defined, membrane delimited organelles such as the myoplasm, sarcoplasmic reticulum, nucleus, or mitochondrion, subsarcolemmal compartments have been considered as functional, with little correspondence to the actual structural organization of the cell (e.g. Standen & Stanfield, 1982; Shiferaw *et al.* 2003; Shannon *et al.* 2004). Here, T-space and M-space are functional compartments; however, their physical characteristics, i.e. size, localization of  $Ca^{2+}$  sensitive proteins (LCC, NCX, RyR), buffers, and  $Ca^{2+}$  fluxes into and out of the compartments were determined based on the structural organization of the porcine ventricular myocyte and using best fit to experimental data. T-space is enclosed by the T-tubules portion of the sarcolemma and the junctional portion of the SR membrane. M-space is enclosed by the non-tubular sarcolemma and the non-junctional SR membrane. LCCs and NCXs reside with different densities in the sarcolemma of T-space and M-space. Note (Fig. 1A) that a portion of the T-tubular membrane can be outside the T-space and LCCs and NCXs there sense M-space  $Ca^{2+}$ .

The effects of the spatial localization of  $I_{NCX}$  on  $Ca_m$  were investigated with a simulated caffeine induced  $J_{rel}$  (Fig. 4). Experiments show that the time course of global  $Ca^{2+}$  lags ( $> 30$  ms) behind  $I_{NCX}$ . Interpretation of this result is not unique and is model dependent. For example, Weber *et al.* (2002) and Trafford *et al.* (1995) showed that the existence of a single diffusion barrier between the subsarcolemmal space (where all  $I_{NCX}$  were located in their models) and the bulk myoplasm is sufficient to account for this phenomenon; the time constant of  $Ca^{2+}$  diffusion flux between the subsarcolemmal space and global myoplasm was used as a fitted parameter in these studies. We used a different approach in this study; instead of fitting the time constant of  $J_{lm}$ , we used the fraction of  $I_{NCX}$  in the T-space,  $\beta$ , as a parameter. Best fit to the experimental data was obtained for 25% of  $I_{NCX}$  in the T-space, 75% of  $I_{NCX}$  in the M-space.

The quantity of sarcolemmal and SR membrane anionic  $Ca^{2+}$  binding sites ('buffers') in the T-space defines the functional 'size' of this compartment. Note that, the effective buffering capacity depends strongly on the kinetics of the buffers (dissociation constants) and not only on the number of available binding sites *per se*. This effective size depends on the membrane surface area that encloses this compartment (which is large) and not on

the myoplasmic volume that it encloses (which is small). The effective size of the T-space compartment depends on the  $\text{Ca}^{2+}$  sensitivity (half-saturation constants) of  $J_{\text{rel}}$ ,  $I_{\text{Ca}}$  and  $I_{\text{NCX}}$ ; it is estimated to be in the range of 0.5–10  $\mu\text{M}$  (units of concentration; Hofer *et al.* 1997; Bers, 2001; Ottolia *et al.* 2009). An increase of sensitivity (i.e. a decrease of half-saturation constants) will increase the effective size of the T-space. In fact the T-space merges with the M-space when the half-saturation constants drop below the average  $\text{Ca}_m$ . A similar merger occurs if  $J_{\text{tm}}$  is large and time to equilibrium between  $\text{Ca}_t$  and  $\text{Ca}_m$  is short.

The use of  $I_{\text{NCX}}$  and  $I_{\text{Ca}}$  as  $\text{Ca}^{2+}$  sensors requires that their sensitivity to  $\text{Ca}^{2+}$  (half-saturation constants,  $K_d$ ) is in the range of expected values of the local  $\text{Ca}^{2+}$  concentration. If the local  $\text{Ca}^{2+}$  concentration is too low ( $\ll K_d$ ) its ability to affect these currents is blunted. Similarly, if it is too high ( $\gg K_d$ ) the dependence of these currents on  $\text{Ca}^{2+}$  reaches saturation and sensitivity is lost.

**Number of compartments in the model.** The representation of the structure in Fig. 1A by the compartmental model in Fig. 1B is not unique. Obviously, during the transition from a 3D structure to a compartmental model certain assumptions must be made. Several studies used three-compartment myoplasmic models (dyads, subsarcolemmal space and bulk myoplasm) or two-compartment models (subsarcolemmal space and bulk myoplasm). Inter-compartmental fluxes and partition of major  $\text{Ca}^{2+}$ -sensitive proteins vary greatly between models. We assumed that regardless of the number of compartments in the model, the total amount of  $\text{Ca}^{2+}$  and total trans-sarcolemmal  $\text{Ca}^{2+}$  flux should be conserved. This conservation relation greatly decreases the parameter space of the model (Livshitz & Rudy, 2009). The strategy to include only two  $\text{Ca}^{2+}$  myoplasmic subcompartments was motivated by the need to ensure that the model is tractable and its parameters are experimentally verifiable. Importantly, it allowed us to formulate an analytic inverse relation between the  $\text{Ca}^{2+}$ -dependent currents ( $I_{\text{Ca}}$  and  $I_{\text{NCX}}$ ) and  $\text{Ca}_t$ .

### Evaluation of methods for estimating $\text{Ca}_t$

We evaluated the validity of the experimental methods for  $\text{Ca}_t$  estimation by simulating the experimental protocols and comparing the inverse-estimated  $\overline{\text{Ca}}_t$  with the model-computed  $\text{Ca}_t$ . The results show that under ideal and fully controlled *in silico* conditions, all methods that use a  $V$ -clamp protocol to activate  $J_{\text{rel}}$  result in similar estimates of  $\text{Ca}_t$ , providing that the SR  $\text{Ca}^{2+}$  load and the depolarizing pulses are the same. Not surprisingly, the amplitude and duration of  $\text{Ca}_t$  induced by

caffeine varies greatly from that induced by depolarization (compare Figs 4–5 and 7–8). Typically,  $\text{Ca}_t$  induced by caffeine has a significantly longer duration than its depolarization-induced counterpart.

**Estimation of  $\text{Ca}_t$  using tail  $I_{\text{NCX}}$  current and  $\text{Ca}_m$ .** We show (Fig. 6) that estimation of  $\text{Ca}_t$  using the  $I_{\text{NCX}}$ -based method provides a good estimate for the descending phase of  $\text{Ca}_t$ . This method is less sensitive to the SR  $\text{Ca}^{2+}$  load than the  $I_{\text{Ca}}$ -based method, as it does not require modulation of the SR  $\text{Ca}^{2+}$  load. The quality of the estimation increases when the number of sampling points increases (duration of testing pulses decreases), a condition that can be difficult to achieve in experiments. An advantage of the  $I_{\text{NCX}}$ -based method is that pharmacological interventions are not required. However, in this method a greater number of parameters must be fitted. Parameter sensitivity analysis indicates that the accuracy is strongly dependent on the specified fraction of  $I_{\text{NCX}}$  in the T-space. In addition, the model used for the estimation should be re-calibrated for each set of ion concentrations ( $\text{Na}_o$ ,  $\text{Ca}_o$ ,  $\text{Na}_i$ ) and test potential  $V$ .

**Estimation of  $\text{Ca}_t$  using  $I_{\text{Ca}}$ .** To derive an analytical expression for  $\text{Ca}_t$  as a function of  $I_{\text{Ca}}$ , several assumptions were made. Since  $J_{\text{rel}}$  provides the dominant contribution to  $\text{Ca}_t$  in ventricular myocytes, its contribution to  $I_{\text{Ca}}$  inactivation (denoted RDI) was used as a surrogate for  $\text{Ca}_t$  (Sham, 1997). To isolate the  $J_{\text{rel}}$ -dependent component from  $I_{\text{Ca}}$  traces, the  $I_{\text{Ca}}$  trace in the absence of  $J_{\text{rel}}$  ( $I_{\text{Ca}}^0$ ) was subtracted from those in the presence of  $J_{\text{rel}}$  (Acsai *et al.* 2011). The  $\Delta I_{\text{Ca}}$ -based method does not depend on the partition of LCCs between the T-space and M-space, because the effects of M-space LCCs is eliminated by the subtraction procedure. We formulated the  $\text{Ca}^{2+}$ -dependent inactivation of  $I_{\text{Ca}}$  as a function of free  $\text{Ca}^{2+}$  concentration assuming that the contributions of  $\text{Ca}^{2+}$  fluxes to changes in the  $\text{Ca}^{2+}$  concentration are additive (eqn (1)). To convert the resulting difference current,  $\Delta I_{\text{Ca}}$  ( $\mu\text{A } \mu\text{F}^{-1}$ ), into the dimensionless units of  $\text{Ca}^{2+}$ -dependent inactivation,  $f_{\text{Ca}}$ , we calibrated  $\Delta I_{\text{Ca}}$  by the value of  $I_{\text{Ca}}^0$  at the time when  $\Delta I_{\text{Ca}}$  reached its maximum (i.e. contribution of  $\text{Ca}_t$  to  $I_{\text{Ca}}$  inactivation was maximal, Fig. 7B). Taking advantage of the completely controlled *in silico* conditions, we simulated a double ( $V$  and  $\text{Ca}^{2+}$ ) clamp protocol (Fig. 7) to study the effect of the delay between depolarization ( $V$  step) and CICR ( $\text{Ca}^{2+}$  pulse) on the relative dynamics of VDI and CDI of  $I_{\text{Ca}}$ . We found that an increased delay between the onset of the  $V$  step and the  $\text{Ca}^{2+}$  step (which can happen under pathophysiological condition that impair  $J_{\text{rel}}$ ; Bito *et al.* 2008) reduced the relative contribution of CDI to total  $I_{\text{Ca}}$  inactivation, even



when the  $\text{Ca}^{2+}$  pulse shape and duration were held constant. Thus, calibrating  $\Delta I_{\text{Ca}}$  by peak  $I_{\text{Ca}}^0$  (eqn (9)) and using the resulting  $\bar{f}_{\text{Ca}}$  as an input to eqn (8) underestimates  $\text{Ca}_t$ . The proposed new calibration procedure does not suffer from this artifact (compare Fig. 7C and D).

The method presented here is based on steady state (time-independent) approximations of  $\text{Ca}^{2+}$ -dependent inactivation of  $I_{\text{Ca}}$  and  $\text{Ca}^{2+}$ -dependent activation of  $I_{\text{NCX}}$ . It was shown that inactivation of  $I_{\text{Ca}}$  induced by  $J_{\text{rel}}$  is a fast process (e.g. Antoons *et al.* 2007; Puglisi *et al.* 1999), especially at high SR  $\text{Ca}^{2+}$  loads (i.e. large  $J_{\text{rel}}$  and  $\text{Ca}_t$ ) and therefore this assumption is well justified. The steady-state approximation allowed us to use an analytic expression for  $\text{Ca}_t$  as a function of  $f_{\text{Ca}}$ . During a voltage pulse, the inverse estimation of  $\text{Ca}_t$  using the  $\Delta I_{\text{Ca}}$ -based method provided the best accuracy at high SR  $\text{Ca}^{2+}$  load, when  $I_{\text{Ca}}$  is sufficiently small relative to  $J_{\text{rel}}$  and does not contribute substantially to  $\text{Ca}_t$ , i.e. when the gain of CICR (i.e.  $J_{\text{rel}}/J_{\text{Ca},t}$  ratio) is high, which is true under normal physiological conditions.

With the  $I_{\text{Ca}}$ -based method, the ascending phase of  $\text{Ca}_t$  is estimated with a greater accuracy than the descending phase (Fig. 8D) (the opposite is true for the  $I_{\text{NCX}}$ -based method). This is an expected result, because this method is based on the  $J_{\text{rel}}$ -component of inactivation and peak  $J_{\text{rel}}$  coincides with the steepest ascending portion of  $\text{Ca}_t$ . However, during the descending portion of  $\text{Ca}_t$  the contribution of  $J_{\text{rel}}$  to inactivation is decreased, resulting in a less accurate estimate. Therefore, combination of the  $I_{\text{Ca}}$  and  $I_{\text{NCX}}$ -based methods provides an estimate for the entire  $\text{Ca}_t$  time course.

### New insights and potential future applications of the model

Beyond estimation of  $\text{Ca}_t$ , the compartmental model presented here provides a conceptual framework for studying the interactions between dynamic  $\text{Ca}^{2+}$ ,  $I_{\text{Ca}}$  and  $I_{\text{NCX}}$  in the functional microdomain where they interact physiologically (T-space). The functional compartmentalization is different from that in previous models; it does not employ a uniform subsarcolemmal 'subspace', but a functional volume near RyR (Acsai *et al.* 2011), where subpopulations of  $I_{\text{Ca}}$  and  $I_{\text{NCX}}$  (estimated here at 90%  $I_{\text{Ca}}$  and 25%  $I_{\text{NCX}}$ ) interact with RyR through a common  $\text{Ca}^{2+}$  pool. The compartmentalization and partition are based on an interpretation of experimental data obtained under voltage clamp conditions and controlled SR  $\text{Ca}^{2+}$  load. For this compartmentalization, we estimated a peak  $\text{Ca}_t$  in the range of 6–25  $\mu\text{M}$ , with time to equilibrium between  $\text{Ca}_t$  and  $\text{Ca}_m$  of about 350 ms. The  $\text{Ca}_t$  values are in the range of LCC and RyR sensitivity to  $\text{Ca}^{2+}$ , which implies that there is a

significant effect of  $\text{Ca}^{2+}$  in this domain on their kinetics and, in turn, on the action potential during physiological cell excitation. A natural continuation of the work presented here will be an implementation and application of the model to study cellular excitation and  $\text{Ca}^{2+}$  cycling under physiological conditions (i.e. an expansion from the controlled, clamped protocols implemented here) and during disease states associated with various pathologies.

## Appendix

### Units and equations

Physical units are as in the original LRd paper (Luo & Rudy, 1994): time ( $t$ ) in milliseconds (ms), membrane voltage ( $V$ ) in millivolts (mV), current through channel X ( $I_X$ ) in microamperes per cell capacitance ( $\mu\text{A } \mu\text{F}^{-1}$ ), channel conductance ( $G_X$ ) and maximal channel conductance ( $\bar{G}_X$ ) in millisiemens per microfarad ( $\text{mS } \mu\text{F}^{-1}$ ), intra-cellular and extracellular ion concentrations ( $X_i$ ,  $X_o$ ) in millimoles per liter (mM). Inter-compartmental  $\text{Ca}^{2+}$  fluxes are defined in terms of millimoles per liter (of the compartment indicated by the first subscript) per millisecond ( $\text{mM ms}^{-1}$ ). Gating variables are given by their steady state and time constant expressions  $x_\infty$  and  $\tau_x$  (ms), or by forward  $\alpha_x$  and backward  $\beta_x$  rate constants ( $\text{ms}^{-1}$ ) as follows:  $dx/dt = (x_\infty - x)/\tau_x = \alpha_x(1 - x) - \beta_x x$ . Model equations and computer code can be found in the research section of <http://rudylab.wustl.edu>. The notations  $\varphi = F/R/T = 0.0374 \text{ (V}^{-1}\text{)}$  and  $\psi = V\varphi$  are used in equations, where  $R = 8314 \text{ (J mol}^{-1} \text{ K}^{-1}\text{)}$  is the universal gas constant,  $F = 96,485$  is the Faraday constant ( $\text{C mol}^{-1}$ ) and  $T = 310$  is the absolute temperature (K);  $z_{\text{Ca}} = 2$  is the valence of  $\text{Ca}^{2+}$  ions.

### Geometrical considerations

Following the LRd model structure (Luo & Rudy, 1994), the M-space volume was set to  $v_m = 25 \times 10^{-6} \mu\text{l}$ , leaving 30% of the total cell volume ( $v_{\text{cell}} = 38\text{e-}6 \mu\text{l}$ ) inaccessible to ions due to the presence of mitochondria and other organelles. The SR volume (6% of  $v_{\text{cell}}$ ) was subdivided into J-space ( $v_j = 0.138\text{e-}6 \mu\text{l}$ ) and N-space ( $v_n = 2.1 \times 10^{-6} \mu\text{l}$ ),  $v_t$  was set conservatively to  $0.38 \times 10^{-6} \mu\text{l}$ , 1% of  $v_{\text{cell}}$ . To ensure  $\text{Ca}^{2+}$  conservation, any change in a compartment volume should be accompanied by a change in the total  $\text{Ca}^{2+}$  concentration. Thus, a decrease of  $v_t$  should be accompanied by a corresponding increase in concentration of  $\text{Ca}^{2+}$  binding sites (buffers) to preserve the total amount of cell  $\text{Ca}^{2+}$ .

Due to cell size variability, experimental recordings of  $I_{\text{Ca}}$  and  $I_{\text{NCX}}$  ( $\mu\text{A } \mu\text{F}^{-1}$ ) were normalized by the total cell capacitance  $C_{\text{cell}}$  ( $\mu\text{F}$ ), which varied from 0.09 to 0.2  $\mu\text{F}$ .



**Table 2. Ca<sup>2+</sup> buffers (Bers, 2001)**

Name of buffer	$k_d = k_-/k_+$ (mM)	$k_-$ (1/ms)	$k_+$ (1/mM ms <sup>-1</sup> )	$\bar{X}$ Maximal concentration (mM)
M-space troponin	0.5e-3	0.02	40	50e-3
M-space calmodulin	2.4e-3	0.24	100	70e-3
T-space fast	0.5e-3	0.05	100	0.7
T-space slow	10e-3	0.1	100	1.32
J-space calsequestrin	0.8	80	100	10

To convert Ca<sup>2+</sup> currents into units of Ca<sup>2+</sup> fluxes, an average value of  $C_{\text{cell}} = 0.15 \mu\text{F}$  was assumed, which is very close to the value used in LRd ( $0.1534 \mu\text{F}$ ). Note that the capacitive areas of the T-tubular and non-tubular portions of the sarcolemma are assumed equal  $C_m = C_t = 0.075 \mu\text{F}$ . Extracellular ion concentrations were set to the values in corresponding experiments.

### Ca<sup>2+</sup> buffering fluxes

The Ca<sup>2+</sup> flux to and from a buffer protein X ( $J_{b,x}$ ) is formulated as a first order kinetic equation:

$$J_{b,x} = \frac{d\text{Ca}_x}{dt} = k_x^+(\bar{X} - \text{Ca}_x) \cdot \text{Ca}_y - k_x^- \text{Ca}_x \quad (\text{A1})$$

where  $\text{Ca}_x$  is bound Ca<sup>2+</sup> to buffer  $x$ ;  $\text{Ca}_y$  is free Ca<sup>2+</sup> in compartment  $y$ . The buffering fluxes in M-space ( $J_{b,m}$ ) include binding–unbinding to troponin and calmodulin Ca<sup>2+</sup> binding sites. The buffering flux in T-space involves fast and slow components ( $J_{b,t} = J_{b,f} + J_{b,s}$ ). These are composed of sarcolemmal anionic binding sites (Post & Langer, 1992), and Ca<sup>2+</sup>/calmodulin binding sites to LCC, RyR and CaMKII (Saucerman & Bers, 2012). Kinetics of the fast and slow buffers were adjusted to best fit  $I_{\text{Ca}}$  inactivation. Volumes of functional Ca<sup>2+</sup> compartments, their buffering capacity, and Ca<sup>2+</sup> fluxes between compartments are interdependent. Therefore, conservation of total cell Ca<sup>2+</sup> was imposed as an additional constraint. Calsequestrin ( $J_{\text{csqn}}$ ) is located in J-space. Forward ( $k_x^+$ ) and backward  $k_x^-$  rate constants and total concentration ( $\bar{X}$ ) of protein X binding sites are summarized in Table 2.

### Ca<sup>2+</sup> flux from J-space to T-space ( $J_{jt}$ )

$J_{jt}$  has two components,  $J_{\text{rel}}$  and  $J_{\text{leak}}$ .  $J_{\text{leak}}$  is an intrinsic RyR Ca<sup>2+</sup> leak, which depends on the Ca<sup>2+</sup> gradient:  $J_{\text{leak}} = k_{\text{leak}}(\text{Ca}_j - \text{Ca}_t)$ . The  $J_{\text{rel}}$  model is based on a previously published model (Livshitz & Rudy, 2007). Following Faber & Rudy (2000),  $J_{\text{rel}}$  is activated by the flux of free Ca<sup>2+</sup> into the T-space, regardless of its origin ( $I_{\text{Ca}}$ ,  $I_{\text{NCX}}$ ,  $I_{\text{tm}}$ ). In addition, to simulate caffeine-induced  $J_{\text{rel}}$ , we included luminal (SR) activation of RyR in the

model. The differential equation that describes  $J_{\text{rel}}$  is of the form:

$$dJ_{\text{rel}}/dt = (J_{\text{rel},\infty} - J_{\text{rel}})/\tau_{\text{rel}} \quad (\text{A2})$$

$J_{\text{rel},\infty} = \alpha_{\text{rel}}(A_{\text{rel}} + B_{\text{rel}})D_{\text{rel}}$  represents the steady-state value of  $J_{\text{rel}}$ ;  $\tau_{\text{rel}} = \beta_{\text{r}}/(1 + K_{\text{rel},\tau}/\text{Ca}_j)$  is the time constant,  $K_{\text{rel},\tau} = 0.0123$ ,  $\beta_{\text{r}} = 4.75$  is the maximal value of  $\tau_{\text{rel}}$ ,  $\alpha_{\text{rel}} = 12 \beta_{\text{r}}$  is the amplitude coefficient.  $J_{\text{rel},\infty}$  is expressed as a product of the sum of cytosolic ( $A_{\text{rel}}$ ) and luminal ( $B_{\text{rel}}$ ) Ca<sup>2+</sup>-dependent activation with luminal deactivation ( $D_{\text{rel}}$ ).  $A_{\text{rel}} = d\text{Ca}_t/dt$  when  $d\text{Ca}_t/dt$  is positive, and  $A_{\text{rel}} = 0$  otherwise. Similarly,  $B_{\text{rel}}$  is not zero only above a certain level of  $\text{Ca}_j$  (threshold). This formulation involves logical expressions that introduce singularities which can cause problems for implementation in a problem solving environment such as MATLAB and for numerical analysis. To remove singularity, we follow the method in Livshitz & Rudy (2009) and introduce an auxiliary function  $\lambda(x) = 1/[1 + \exp(-x\gamma)]$ , where  $\gamma$  is a small (e.g.  $1 \times 10^{-8}$ ) number.  $\lambda(x)$  is equal to unity for a positive argument and zero otherwise. Formulations of  $A_{\text{rel}}$  and  $B_{\text{rel}}$  in terms of  $\lambda(x)$  are  $A_{\text{rel}} = (d\text{Ca}_t/dt) \cdot \lambda(d\text{Ca}_t/dt)$  and  $B_{\text{rel}} = \lambda(\text{Threshold} - \text{Ca}_j)$ .  $\text{Ca}_j$ -dependent deactivation was modelled as a steep saturating function of  $\text{Ca}_j$ :  $D_{\text{rel}} = 1/[1 + (K_{\text{rel},\infty}/\text{Ca}_j)^h]$ , where  $K_{\text{rel},\infty} = 1 \text{ mM}$  is the half-saturation coefficient and  $h = 9$ . Application of caffeine was simulated by a gradual decrease of  $K_{\text{rel},\infty}$  to zero, and by simultaneous increase of  $\alpha_{\text{rel}}$  and  $k_{\text{leak}}$ .

### $J_{mn}$ (bidirectional) flux between the M-space and the N-space

$J_{mn}$  is described by a phenomenological equation, as proposed in Shannon *et al.* (2004)

$$J_{mn} = \bar{J}_{\text{SERCA}} \frac{(\text{Ca}_m/K_{\text{up}})^h - (\text{Ca}_n/n\text{SR})^h}{1 + (\text{Ca}_m/K_{\text{up}})^h + (\text{Ca}_n/n\text{SR})^h} - k_{\text{leak}}(\text{Ca}_n - \text{Ca}_m) \quad (\text{A3})$$

$n\text{SR}$  (maximal affinity to SR Ca) = 15 mM,  $\bar{J}_{\text{SERCA}} = 0.875 \times 10^{-3} \text{ mM ms}^{-1}$ ,  $K_{\text{up}} = 0.8 \times 10^{-3} \text{ mM}$ ,  $h = 1.7$ .

## References

- Adachi-Akahane S, Cleemann L & Morad M (1996). Cross-signaling between L-type  $\text{Ca}^{2+}$  channels and ryanodine receptors in rat ventricular myocytes. *J Gen Physiol* **108**, 435–454.
- Adler D, Wong AY & Mahler Y (1985). Model of mechanical alternans in the mammalian myocardium. *J Theor Biol* **117**, 563–577.
- Adrian RH (1983). Electrical properties of striated muscle. In *Handbook of Physiology*, section 10, *Skeletal Muscle*, ed. Peachy L, pp. 275–300. American Physiological Society, Bethesda, MD.
- Acsai K, Antoons G, Livshitz L, Rudy Y & Sipido KR (2011). Assessment of  $[\text{Ca}^{2+}]$  near ryanodine receptors during sarcoplasmic reticulum  $\text{Ca}^{2+}$  release with L-type  $\text{Ca}^{2+}$  and Na/Ca exchange currents as  $[\text{Ca}^{2+}]$  reporter. *J Physiol* **589**, 2569–2583.
- Allbritton NL, Meyer T & Stryer L (1992). Range of messenger action of calcium ion and inositol 1,4,5-trisphosphate. *Science* **258**, 1812–1815.
- Antoons G, Volders PGA, Stankovicova T, Bito V, Stengl M, Vos MA & Sipido KR (2007). Window  $\text{Ca}^{2+}$  current and its modulation by  $\text{Ca}^{2+}$  release in hypertrophied cardiac myocytes from dogs with chronic atrioventricular block. *J Physiol* **579**, 147–160.
- Atkins GL (1969). *Multicompartment Models for Biological Systems*. Methuen & Co. Ltd., London.
- Belevych AE, Terentyev D, Terentyeva R, Nishijima Y, Sridhar A, Hamlin RL, Carnes CA & Györke S (2011). The relationship between arrhythmogenesis and impaired contractility in heart failure: role of altered ryanodine receptor function. *Cardiovasc Res* **90**, 493–502.
- Bers DM (2001). *Excitation–Contraction Coupling and Cardiac Contractile Force*. Kluwer Academic Publishers, Dordrecht.
- Bito V, Heinzel FR, Biesmans L, Antoons G & Sipido KR (2008). Crosstalk between L-type  $\text{Ca}^{2+}$  channels and the sarcoplasmic reticulum: alterations during cardiac remodeling. *Cardiovasc Res* **77**, 315–324.
- Blinks JR, Olson CB, Jewell BR & Braveny P (1972). Influence of caffeine and other methylxanthines on mechanical properties of isolated mammalian heart muscle. *Circ Res* **30**, 367–392.
- Bootman MD, Higazi DR, Coombes S & Roderick HL (2006). Calcium signalling during excitation-contraction coupling in mammalian atrial myocytes. *J Cell Sci* **119**, 3915–3925.
- Bondarenko VE, Szigeti GP, Bett GCL, Kim S-J & Rasmusson RL (2004). Computer model of action potential of mouse ventricular myocytes. *Am J Physiol Heart Circ Physiol* **287**, H1378–H1403.
- Chen-Izu Y, McCulle SL, Ward CW, Soeller C, Allen BM, Rabang C, Cannell MB, Balke CW & Izu LT (2006). Three dimensional distribution of ryanodine receptor clusters in cardiac myocytes. *Biophys J* **91**, 1–13.
- Drummond GB (2009). Reporting ethical matters in *The Journal of Physiology*: standards and advice. *J Physiol* **587**, 713–719.
- Egan TM, Noble D, Noble SJ, Powell T, Spindler AJ & Twist VW (1989). Sodium-calcium exchange during the action potential in guinea-pig ventricular cells. *J Physiol* **411**, 639–661.
- Faber GM, Silva J, Livshitz L & Rudy Y (2007). Kinetic properties of the cardiac L-type Ca channel and its role in myocyte electrophysiology: A theoretical investigation. *Biophys J* **92**, 1522–1543.
- Faber GM & Rudy Y (2000). Action potential and contractility changes in  $[\text{Na}^+]_i$  overloaded cardiac myocytes: a simulation study. *Biophys J* **78**, 2392–2404.
- Greenstein JL, Hinch R & Winslow RL (2006). Mechanisms of excitation-contraction coupling in an integrative model of the cardiac ventricular myocyte. *Biophys J* **90**, 77–91.
- Gaur N & Rudy Y (2011). Multiscale modeling of calcium cycling in cardiac ventricular myocyte: macroscopic consequences of microscopic dyadic function. *Biophys J* **100**, 2904–2912.
- Hadley RW & Hume JR (1987). An intrinsic potential dependent inactivation mechanism associated with calcium channels in guinea-pig myocytes. *J Physiol* **389**, 205–222.
- Hille B (2001). *Ion Channels of Excitable Membranes*, 3rd edn. Sinauer Associates, Inc. Sunderland, MA, USA.
- Heinzel FR, Bito V, Volders PG, Antoons G, Mubagwa K & Sipido KR (2002). Spatial and temporal inhomogeneities during  $\text{Ca}^{2+}$  release from the sarcoplasmic reticulum in pig ventricular myocytes. *Circ Res* **91**, 1023–1030.
- Hund TJ & Rudy Y (2004). Rate dependence and regulation of action potential and calcium transient in a canine cardiac ventricular cell model. *Circulation* **110**, 3168–3174.
- Higgins ER, Goel P, Puglisi JL, Bers DM, Cannell M & Sneyd J (2007). Modelling calcium microdomains using homogenisation. *J Theor Biol* **247**, 623–644.
- Kass RS & Sanguinetti MC (1984). Inactivation of calcium channel current in the calf cardiac Purkinje fiber. *J Gen Physiol* **84**, 705–726.
- Hofer GF, Hohenthanner K, Baumgartner W, Groschner K, Klugbauer N, Hofmann F & Romanin C (1997). Intracellular  $\text{Ca}^{2+}$  inactivates L-type  $\text{Ca}^{2+}$  channels with a Hill coefficient of approximately 1 and an inhibition constant of approximately 4  $\mu\text{M}$  by reducing channel's open probability. *Biophys J* **73**, 1857–1865.
- Keller JB (1976). Inverse problems. *Am Math Monthly* **83**, 107–118.
- Kong H, Jones PP, Koop A, Zhang L, Duff HJ & Chen SRW (2008). Caffeine induces  $\text{Ca}^{2+}$  release by reducing the threshold for luminal  $\text{Ca}^{2+}$  activation of the ryanodine receptor. *Biochem J* **414**, 441–452.
- Jayasinghe ID, Cannell MB & Soeller C (2009). Organization of ryanodine receptors, transverse tubules, and sodium-calcium exchanger in rat myocytes. *Biophys J* **97**, 2664–2673.
- Langer GA & Peskoff A (1998). Calcium concentration and movement in the ventricular cardiac cell during an excitation-contraction cycle. *Biophys J* **74**, 153–174.
- Lee KS, Marban E & Tsien RW (1985). Inactivation of calcium channels in mammalian heart cells: joint dependence on membrane potential and intracellular calcium. *J Physiol* **364**, 395–411.
- Li P & Rudy Y (2011). A model of canine purkinje cell electrophysiology and  $\text{Ca}^{2+}$  cycling. *Circ Res* **109**, 71–79.
- Livshitz LM & Rudy Y (2007). Regulation of Ca and electrical alternans in cardiac myocytes: role of CAMKII and repolarizing currents. *Am J Physiol Heart Circ Physiol* **292**, H2854–H2866.

- Livshitz LM & Rudy Y (2009). Uniqueness and stability of action potential models during rest, pacing and conduction using problem solving environment. *Biophys J* **97**, 1265–1276.
- Luo CH & Rudy Y (1994). A dynamic model of the cardiac ventricular action potential. Simulations of ionic currents and concentration changes. *Circ Res* **74**, 1071–96.
- Mahajan A, Shiferaw Y, Sato D, Baher A, Olcese R, Xie L-H, Yang M-J, Chen P-S, Restrepo JG, Karma A, Garfinkel A, Qu Z & Weiss JN (2008). A rabbit ventricular action potential model replicating cardiac dynamics at rapid heart rates. *Biophys J* **94**, 392–410.
- Melzer W, Rios E & Schneider MF (1987). A general procedure for determining the rate of calcium release from the sarcoplasmic reticulum in skeletal muscle fibers. *Biophys J* **51**, 849–863.
- Morad M & Soldatov N (2005). Calcium channel inactivation: Possible role in signal transduction and  $\text{Ca}^{2+}$  signalling. *Cell Calcium* **38**, 223–231.
- Naraghi M & Neher E (1997). Linearized buffered  $\text{Ca}^{2+}$  diffusion in microdomains and its implications for calculation of  $[\text{Ca}^{2+}]$  at the mouth of a calcium channel. *J Neuroscience* **17**, 6961–6973.
- Ottolia M, Nicoll DA & Philipson KD (2009). Roles of two  $\text{Ca}^{2+}$ -binding domains in regulation of the cardiac  $\text{Na}^{+}$ – $\text{Ca}^{2+}$  exchanger. *J Biol Chem* **284**, 32735–32741.
- Pasek M, Brette F, Nelson A, Pearce C, Qaiser A, Christe G & Orchard CH (2008). Quantification of t-tubule area and protein distribution in rat cardiac ventricular myocytes. *Prog Biophys Mol Biol* **96**, 244–257.
- Priori SG & Chen SR (2011). Inherited dysfunction of sarcoplasmic reticulum  $\text{Ca}^{2+}$  handling and arrhythmogenesis. *Circ Res* **108**, 871–883.
- Puglisi J, Yuan W, Bassani J & Bers DM (1999).  $\text{Ca}^{2+}$  influx through  $\text{Ca}^{2+}$  channels in rabbit ventricular myocytes during action potential clamp -Influence of temperature. *Circ Res* **85**, E7–E16.
- Post JA & Langer GA (1992). Sarcolemmal calcium binding sites in heart. I. Molecular origin in “gas-dissected” sarcolemma. *J Membr Biol* **129**, 49–57.
- Reeves JP & Condrescu M (2003). Allosteric activation of sodium–calcium exchange activity by calcium: persistence at low calcium concentrations. *J Gen Physiol* **122**, 621–639.
- Sato D, Shiferaw Y, Garfinkel A, Weiss JN, Qu Z & Karma A (2006). Spatially discordant alternans in cardiac tissue: Role of calcium cycling. *Circ Res* **99**, 520–527.
- Saucerman & Bers (2012). Calmodulin binding proteins provide domains of local  $\text{Ca}^{2+}$  signaling in cardiac myocytes. *J Mol Cell Cardiol* **52**, 312–316.
- Sipido KR & Wier WG (1991). Flux of  $\text{Ca}^{2+}$  across the sarcoplasmic guinea-pig cardiac cells during excitation–coupling. *J Physiol* **435**, 605–663.
- Sipido KR, Callewaert G & Carmeliet E (1995). Inhibition and rapid recovery of ICa during calcium release from the sarcoplasmic reticulum in guinea-pig ventricular myocytes. *Circ Res* **76**, 102–109.
- Shiferaw Y, Watanabe MA, Garfinkel A, Weiss JN & Karma A (2003). Model of intracellular calcium cycling in ventricular myocytes. *Biophys J* **85**, 3666–3686.
- Smyrniasi I, Maira W, Harzheim D, Walkera SAHL & Bootman MD (2010). Comparison of the T-tubule system in adult rat ventricular and atrial myocytes, and its role in excitation-contraction coupling and inotropic stimulation. *Cell Calcium* **47**, 210–223.
- Soeller C, Crossman D, Gilbert R & Cannell MB (2007). Analysis of ryanodine receptor clusters in rat and human cardiac myocytes. *Proc Natl Acad Sci U S A* **104**, 14958–14963.
- Soeller C, Jayasinghe ID, Li P, Holden AV & Cannell MB (2009). Three-dimensional high-resolution imaging of cardiac proteins to construct models of intracellular  $\text{Ca}^{2+}$  signalling in rat ventricular myocytes. *Exp Physiol* **94**, 496–508.
- Sham JSK (1997).  $\text{Ca}^{2+}$  release-induced inactivation of  $\text{Ca}^{2+}$  current in rat ventricular myocytes: Evidence for local  $\text{Ca}^{2+}$  signalling. *J Physiol* **500**, 285–295.
- Shannon TR, Wang F, Puglisi JL, Weber C & Bers DM (2004). A mathematical treatment of integrated  $\text{Ca}^{2+}$  dynamics within the ventricular myocyte. *Biophys J* **87**, 3351–3371.
- Standen NB & Stanfield PR (1982). A binding-site model for calcium channel inactivation that depends on calcium entry. *Proc R Soc Lond B Biol Sci* **217**, 101–110.
- Stengl M, Bartak F, Sykora R, Chvojka J, Benes J, Krouzecky A, Novak I, Svirglerova J, Kuncova J & Matejovic M (2010). Reduced L-type calcium current in ventricular myocytes from pigs with hyperdynamic septic shock. *Crit Care Med* **38**, 579–587.
- Stern MD (1992). Theory of excitation-contraction coupling in cardiac muscle. *Biophys J* **63**, 497–517.
- Trafford AW, Diaz ME, O'Neill SC & Eisner DA (1995). Comparison of subsarcolemmal and bulk calcium-concentration during spontaneous calcium-release in rat ventricular myocytes. *J Physiol* **488**, 577–586.
- Weber C, Piacentino V, Ginsburg K, Houser S & Bers DM (2002).  $\text{Na}^{+}$ – $\text{Ca}^{2+}$  exchange current and submembrane  $[\text{Ca}^{2+}]$  during the cardiac action potential. *Circ Res* **90**, 182–189.
- Weber C, Ginsburg K, Philipson K, Shannon T & Bers DM (2001). Allosteric regulation of Na/Ca exchange current by cytosolic Ca in intact cardiac myocytes. *J Gen Physiol* **117**, 119–131.
- Winkla LL, Sheng-Yong Wang & Langer GA (1999). Subcellular  $\text{Ca}^{2+}$  distribution with varying  $\text{Ca}^{2+}$  load in neonatal cardiac cell culture. *Biophys J* **76**, 2649–2663.
- Zahradnikova A, Kubalova Z, Pavelkova J, Gyorke S & Zahradnik I (2004). Activation of calcium release assessed by calcium release-induced inactivation of calcium current in rat cardiac myocytes. *Am J Physiol Cell Physiol* **286**, C330–C341.

### Author contributions

L.L. participated in data analysis, provided the theoretical basis for the computations, and contributed to manuscript writing. K.A. performed experiments and data analysis and participated in manuscript writing. K.A. developed the computational methods together with L.L. and Y.R. G.A. performed experiments and data analysis and participated in manuscript writing. K.S. contributed to the experimental study design and the final manuscript writing. Y.R. participated in data

analysis, provided the theoretical basis for the computations, and participated in manuscript writing. All authors approved the final version of the manuscript. The experimental work was conducted at the laboratory in Leuven, Belgium, with additional analysis performed at the University of Szeged and at Washington University in St Louis.

### Acknowledgements

This research was supported by the NIH–National Heart, Lung and Blood Institute Grants R01-HL049054-19 and R01-HL033343-27 (to Y.R.). This material is based upon

work supported in part by the National Science Foundation under Grant No. CBET-0929633. Any opinions, findings and conclusions or recommendations expressed in this material are those of the authors and do not necessarily reflect the views of the National Science Foundation (NSF). The work was also supported in part by the Fondation Leducq Award to the Alliance for Calmodulin Kinase Signalling in Heart Disease (to K.R.S. and Y.R.). Y.R. is the Fred Saigh Distinguished Professor at Washington University. This study was funded by grants from the Belgian Science Policy Program P6/31 and European Union grant Health-F2-2009-241526 EUTrigTreat (to K.R.S.).